U–Pb geochronology of epidote by LA–ICP–MS as a tool for dating hydrothermal-vein formation

Veronica Peverelli[1], Tanya Ewing[1], Daniela Rubatto[1], Martin Wille[1], Alfons Berger[1], Igor Maria Villa[1,2], Pierre Lanari[1], Thomas Pettke[1], Marco Herwegh[1]

5 [1]Institute of Geological Sciences, University of Bern, Bern, 3012, Switzerland
[2]Dipartimento di Scienze dell'Ambiente e della Terra, University of Milano-Bicocca, Milan, 20126, Italy

Correspondence to: Veronica Peverelli (veronica.peverelli@geo.unibe.ch)

Abstract. Epidote – here defined as minerals belonging to the epidote–clinozoisite solid solution – is a low-μ (μ = $^{238}U/^{204}Pb$) mineral occurring in a variety of geological environments, participating in many metamorphic reactions and

10 stable throughout a wide range of pressure–temperature conditions. Despite containing fair amounts of U, its use as a U–Pb geochronometer has been hindered by the commonly high contents of initial Pb with isotopic compositions that cannot be assumed a priori. We present U–Pb geochronology of hydrothermal-vein epidote spanning a wide range of Pb (3.9–190 µg g^{-1}), Th (0.01–38 µg g^{-1}) and U (2.6–530 µg g^{-1}) contents and with μ values between 7–510 from the Albula area (eastern Swiss Alps), from the Grimsel area (central Swiss Alps) and from the Heyuan fault (Guangdong province, China). The

15 investigated epidote samples show appreciable fractions of initial Pb contents (f_{206} = 0.7–1.0) – i.e. relative to radiogenic Pb – that vary to different extents. A protocol has been developed for in situ U–Pb dating of epidote by spot-analysis laser ablation inductively coupled plasma mass spectrometry (LA–ICP–MS) with a magmatic allanite as primary reference material. The suitability of the protocol and the reliability of the measured isotopic ratios have been ascertained by independent measurements of $^{238}U/^{206}Pb$ and $^{207}Pb/^{206}Pb$ ratios respectively by quadrupole and multicollector ICP–MS

20 applied to epidote micro-separates digested and diluted in acids. For age calculation, we used the Tera–Wasserburg ($^{207}Pb/^{206}Pb$ versus $^{238}U/^{206}Pb$) diagram, which does not require corrections for initial Pb and provides the initial $^{207}Pb/^{206}Pb$ ratio. Petrographic and microstructural data indicate that the calculated ages date the crystallization of vein epidote from a hydrothermal fluid and that the U–Pb system was not reset to younger ages by later events. Vein epidote from the Albula area formed in the Paleocene (62.7 ± 3.0 Ma) and is related to Alpine greenschist-facies metamorphism. The Miocene (19.2

25 ± 4.3 Ma and 16.9 ± 3.7 Ma) epidote veins from the Grimsel area formed during the Handegg deformation phase (22–17 Ma) of the Alpine evolution of the Aar Massif. Identical initial $^{207}Pb/^{206}Pb$ ratios reveal homogeneity in Pb isotopic compositions of the fluid across ca. 100 m. Vein epidote from the Heyuan fault is Cretaceous in age (107.2 ± 8.9 Ma) and formed during the early movements of the fault. In situ U–Pb analyses of epidote returned reliable ages of otherwise undatable epidote-quartz veins. The Tera–Wasserburg approach has proven pivotal for in situ U–Pb dating of epidote and the decisive aspect

30 for low age uncertainties is the variability in intra-sample initial Pb fractions.

1 Introduction

Linking petrological and structural information to the timing of geological events is crucial to better constrain the sequence of geodynamic processes. In this context, the role of fluids in the continental crust is particularly relevant because they mediate and influence deformation and metamorphism (e.g. Wyllie, 1977; Etheridge et al., 1983; Johannes, 1984; Pennacchioni and Cesare, 1997; Malaspina et al., 2011; Wehrens et al., 2016). The formation of a hydrothermal vein represents a specific deformation and hydration event in the geological history of the host rock, during which the vein-filling minerals record the geochemical signature of the mineralizing fluid (e.g. Elburg et al., 2002; Barker et al., 2009; Bons et al., 2012; Parrish et al., 2018; Ricchi et al., 2019; 2020). By combining different geochemical and geochronological techniques to suitable vein-filling minerals it is therefore possible to determine when the vein formed and the isotopic signature of the fluids for insight into their origin (e.g. Pettke et al., 2000; Barker et al., 2006; Elburg et al., 2002).

The epidote–clinozoisite solid solution [$Ca_2Al_3Si_3O_{12}(OH)$–$Ca_2Al_2Fe^{3+}Si_3O_{12}(OH)$], hereafter referred to as epidote, produces common rock-forming and vein-filling minerals (e.g. Bird and Spieler, 2004; Franz and Liebscher, 2004; Guo et al., 2014; Zanoni et al., 2016). Epidote is stable over a wide range of pressure–temperature conditions and in a multitude of magmatic, metamorphic and hydrothermal mineral assemblages (Bird and Spieler, 2004; Enami et al., 2004; Grapes and Hoskin, 2004; Schmidt and Poli, 2004). Its complex crystal structure incorporates a large variety of elements, enabling the measurements of trace element (e.g. Frei et al., 2004) and isotopic (e.g. Guo et al., 2014) signatures. Uranium and thorium are readily accepted into the epidote structure, with contents that are highly variable but generally in trace element levels (Frei et al., 2004). Hence, attempts have been made at using it as a geochronometer by step-wise leaching Pb–Pb dating (e.g. Buick et al., 1999) and thermal ionization mass spectrometry (TIMS) U–Pb dating (e.g. Oberli et al., 2004). Buick et al. (1999) constrained the timing of vein formation and that of subsequent fluid pulses in garnet-epidote-quartz veins in the Reynolds Range (central Australia). Oberli et al. (2004; their Sect. 5.3 and their Fig. 5) obtained a U–Pb age of magmatic epidote from the Bergell pluton (eastern Central Alps) and identified epidote formation as a late-stage process during the solidification of the pluton. However, these techniques allow microstructural control only if sampling by micro-drilling is viable. Epidote could provide valuable geochronological and isotopic information where no other datable minerals are available. Good examples are epidote-quartz veins that are widespread in the Alps (e.g. Aar Massif and Albula area). Syn-kinematic epidote in breccias associated with rift-related faults in the Campos basin (southeastern Brazil) may highlight successive phases of fault movement (Savastano et al., 2017). In the Zermatt-Saas Zone (Western Alps), epidote is a peak-pressure rock-forming mineral in epidote-bearing rodingites (Zanoni et al., 2016) and it may help to better constrain the P–T–d–t paths related to pressure-peak metamorphism.

This contribution discusses the applicability of in situ U–Pb dating to minerals compositionally within the epidote–clinozoisite solid solution. To our knowledge, no analytical protocols have been proposed in this respect. To fill this gap, we present U–Pb ages measured in hydrothermal-vein epidote by LA–ICP–MS using a magmatic allanite for standardization, following a protocol similar to that applied to apatite U–Pb dating (e.g. Odlum and Stockli, 2019; 2020). The main issues

related to the proposed geochronometer and addressed in this contribution are 1) the suitability of magmatic allanite as the most closely matrix-matched reference material for LA–ICP–MS U–Pb dating of epidote in spot-analysis mode, 2) the applicability of the protocol with respect to the different contents of initial Pb fractions (i.e. relative to radiogenic Pb in total Pb) and U in the studied samples and 3) the effects on age precision of the interplay between analyzed volumes and preservation of chemical variability. The Tera–Wasserburg diagram proves to be the key tool for successful epidote U–Pb geochronology, allowing to add minerals of the epidote–clinozoisite solid solution to the list of low-μ U–Pb geochronometers. Notably, by investigating epidote on its own, it is possible to combine U–Pb ages and isotopic systematics with data from trace element analyses and other isotopic systems; this may permit to reconstruct fluid flow and its origin with information that is all provided by a single mineral.

1.1 The challenges of investigating epidote as a geochronometer

Along with relevant amounts of U^{4+} and Th^{4+} as Ca substitution in the A site and of U^{6+} as Al or Fe substitution in the M site (Frei et al., 2004), high contents of initial Pb are incorporated by epidote during crystallization. This causes the dilution of ingrown radiogenic Pb, whose precise measurements are imperative for U–Pb geochronology, and makes epidote a low parent-to-daughter or low-μ phase (i.e. $\mu <$ ca. 2000; Romer, 2001; Romer and Xiao, 2005). U–Pb dating of initial Pb-rich minerals can proceed in two ways depending on whether or not the isotopic composition of the initial Pb is known or can be reasonably assumed. Assumptions can be based on the modeled evolution of global Pb isotopic compositions such as those proposed by Cumming and Richards (1975) and Stacey and Kramers (1975). In the first case, a correction for initial Pb can be applied, and an initial Pb-corrected U–Pb age can be calculated from the measured U($\pm$Th)–Pb isotopic ratios of each analysis (Williams, 1998). However, age inaccuracies due to wrong assumptions regarding initial Pb isotopic compositions can be significant (see Romer, 2001; Romer and Xiao, 2005). An initial Pb-correction can be applied if the contents of ^{204}Pb – the only non-radiogenic lead isotope – can be measured precisely, which is not always the case (e.g. because of the analytical technique employed). Hence, if no other dating method is viable (e.g. too low Th contents hampering Th–Pb dating), the best solution for dating of low-μ phases is to use a regression through the analyses uncorrected for initial Pb on the Tera–Wasserburg diagram (Tera and Wasserburg, 1972), which plots measured ^{207}Pb/^{206}Pb versus ^{238}U/^{206}Pb ratios. Its advantages are that 1) it does not require corrections for initial Pb isotopic compositions, 2) it provides the initial ^{207}Pb/^{206}Pb ratio itself in addition to an initial Pb-corrected U–Pb age, and 3) it gives an estimate of the fractions of initial lead relative to those of radiogenic Pb in each analysis (Tera and Wasserburg, 1972; Ludwig, 1998). This approach is based on the hypotheses that multiple analyses are performed on material of the same age sharing the same initial Pb isotopic composition. If these criteria are met, one regression is defined by the alignment of the measurements of ^{207}Pb/^{206}Pb vs. ^{238}U/^{206}Pb ratios, whose lower intercept with the concordia yields the age of the sample. If the hypotheses prove to be wrong (e.g. multiple mineral generations or co-genetic minerals with different initial Pb isotopic compositions; e.g. Romer and Siegesmund, 2003), this is highlighted by the statistical parameters of the regression. The fraction of initial Pb in each analysis can be estimated from the proximity of individual data points to the upper ^{207}Pb/^{206}Pb intercept of the regression

(Tera and Wasserburg, 1972; Ludwig, 1998) which gives the initial $^{207}Pb/^{206}Pb$ ratio of the sample. The regression in the Tera–Wasserburg diagram is better constrained and yields more precise ages if the variability in initial Pb and U contents is high enough to produce spread-out data points. Epidote minerals are commonly characterized by chemical zoning (Franz and Liebscher, 2004), which may also result in variability in initial Pb fractions and U contents and promote spread of the data points along the Tera–Wasserburg regression.

A suitable technique for in situ U–Th–Pb dating is LA–ICP–MS in spot-analysis mode, provided that U/Pb and Th/Pb elemental fractionation at the ablation site (downhole fractionation, DF) is appropriately corrected for over ablation time by relying on an external reference material (e.g. Sylvester, 2005; Košler, 2007; McFarlane et al., 2016). Since DF is matrix dependent (e.g. Sylvester, 2005; Košler, 2007; Sylvester, 2008; El Korh, 2014), a matrix-matched reference material is most commonly used. To date, no reference epidote exists, posing the problem of correction for DF of $^{238}U/^{206}Pb$ ratios measured in epidote, crucial for accurate age determinations by LA–ICP–MS (Horstwood et al., 2016). One way to date epidote by LA–ICP–MS would be by dynamic (raster) ablation with a non-matrix-matched reference material (e.g. Darling et al., 2012). However, large-enough areas within epidote grains are frequently not available for dynamic ablation. A mineral with a matrix that closely matches that of epidote is allanite. After early work by ID–TIMS (e.g. Barth et al., 1994), magmatic allanite has been dated by SIMS (e.g. Catlos et al., 2000) and in recent years it has been successfully characterized and dated by U–Th–Pb LA–ICP–MS (e.g. Gregory et al., 2007; 2012; El Korh, 2014; Smye et al., 2014). Several allanite samples have been proposed as suitable primary reference materials for LA–ICP–MS dating (e.g. Gregory et al., 2007; Smye et al., 2014). Allanite $[(Ca, REE, Th)_2(Fe^{3+}, Al)_3Si_3O_{12}(OH)]$ is the REE-rich member of the epidote mineral group with ThO_2 contents of 2–3 wt% and U concentrations often below 1000 ppm (Gieré and Sorensen, 2004; and references therein), and it is a promising candidate as a closely matrix-matched reference material for minerals of the epidote–clinozoisite solid solution. The possible issues in the use of allanite as reference material for accurate U–Th–Pb geochronology are mostly related to local isotopic heterogeneity, excess ^{206}Pb due to incorporation of ^{230}Th during crystallization, variable contents of initial Pb and disturbance of the geochronometer by secondary processes (e.g. hydrothermal alteration; Gregory et al., 2007; Darling et al., 2012; Smye et al., 2014; Burn et al., 2017). Nevertheless, these issues can be largely avoided by careful selection of spot analyses referring to backscattered electron (BSE) images, and by identifying and excluding problematic analyses from calculations.

A disadvantage of U–Pb analyses by LA–ICP–MS is the large isobaric interference on mass 204 by ^{204}Hg of the carrier gas. A correction for such an interference in order to apply a ^{204}Pb-correction – whether based on measurements of the initial Pb isotopic composition in the same mineral or in coexisting ones (e.g. Cenki-Tok et al., 2014) – is complex (e.g. Storey et al., 2006). For this reason, and considering that epidote-bearing veins may not include other minerals suitable to determine the initial Pb isotopic composition, the application of the Tera–Wasserburg approach is preferable. In this study, epidote ages and initial $^{207}Pb/^{206}Pb$ ratios are assessed from the Tera–Wasserburg diagram. If initial $^{207}Pb/^{206}Pb$ ratios are consistent with modeled values of initial Pb isotopic compositions (e.g. Stacey and Kramers, 1975), then an accurate $^{238}U/^{206}Pb$ age can be

130 obtained by averaging single-spot ages, which are calculated from each analysis corrected for initial Pb by applying a [207]Pb-correction (i.e. weighted average [207]Pb-corrected [238]U/[206]Pb age; see Williams, 1998).

2 Geological context and field relations

Hydrothermal epidote veins (Fig. 1) were sampled at Albula Pass (eastern Swiss Alps), at Grimsel Pass (central Swiss Alps) and at the Heyuan Fault (Guangdong Province, China). Although there are no precise anticipated ages for the selected
135 epidote samples, the well-constrained tectonic histories of the sampling areas and of the lithologies hosting the studied epidote-bearing veins allow to verify whether or not the obtained ages are geologically reasonable.

The Albula area is located in the upper Err nappe, close to the tectonic contact with the Ela nappe. It belongs to the Austroalpine domain, the basement of the former Adriatic continental margin (e.g. Froitzheim and Eberli, 1990; Froitzheim et al., 1994). The most common lithology in the Err basement is the Albula Granite, a granodiorite of Variscan to post-
140 Variscan age (e.g. Manatschal and Nievergelt, 1997; Incerpi et al., 2017) and in which epidote ± quartz veins are widespread. In the late Carboniferous and early Permian, the Albula Granite intruded into the metamorphic basement of the Err nappe at < 3 km depth (Mohn et al., 2011; and references therein). Subsequently, the Lower Austroalpine was involved in the Jurassic rifting that led to the break-up of Pangea (e.g. Manatschal et al., 2000). During the Alpine orogeny, the Err nappe mainly recorded the deformation resulting from the W- to NW-directed vergence of the Austroalpine domain from Cretaceous until
145 early Cenozoic times and was only weakly affected by the Cenozoic tectonics, when temperatures reached ca. 300 °C (i.e. lower-greenschist facies conditions; e.g. Froitzheim and Manatschal, 1996; Mohn et al., 2011; Epin et al., 2017). Sample Albula-1 was collected at coordinates 46°34'36"N/9°48'06"E and has not been described in previous studies.

The Grimsel area is in the Aar Massif, one of the External Crystalline Massifs of the Alps (Rolland et al., 2009; Wehrens et al., 2017; Herwegh et al., 2020). Here, epidote-quartz veins are common in the Central Aar granite and in the Grimsel
150 granodiorite, which during the earliest Permian intruded into a polycyclic basement bearing evidence of Ordovician metamorphism and Variscan overprint (Schaltegger and Corfu, 1992; Berger et al., 2017). After being affected by the Jurassic rifting, the Aar Massif was involved in the continent–continent collision during the Alpine orogeny, as demonstrated by the presence of anastomosing high-strain shear zones of Alpine age (e.g. Goncalves et al., 2012; Wehrens et al., 2017). Metamorphism at greenschist facies conditions reached 450 ± 30 °C at 0.6 ± 0.1 kbar in this area (Challandes et al., 2008;
155 Goncalves et al., 2012). The Alpine history of the Aar Massif is subdivided into three phases: 1) the Handegg phase (22–17 Ma; Challandes et al., 2008), with stable green biotite in the shear zones (Challandes et al., 2008; Rolland et al., 2009; Herwegh et al., 2017; Wehrens et al., 2017); 2) the Oberaar phase in the southern Aar Massif (14–3.4 Ma; Hofmann et al., 2004; Rolland et al., 2009), with white mica and chlorite stable in the shear zones, and metastable biotite (Herwegh et al., 2017; Wehrens et al., 2017); 3) the Pfaffenchopf phase in the northern Aar Massif (< 12 Ma; Herwegh et al., 2020). The
160 epidote-quartz veins analyzed in this study were sampled in the Nagra Felslabor tunnel at Grimsel Pass. As these veins are only visible within the tunnel, their relationships with Alpine structures and between each other are not known. Samples

Grimsel-1 and Grimsel-2 have not been previously described and they were sampled at a distance of ca. 100 m from each other, close to the "F100" and "BK cavern" locations in Fig. 1.2 of Schneeberger et al. (2019), respectively.

The Heyuan Fault is a crustal-scale fault that formed in Mesozoic times as a low-angle normal fault, but is currently active under a transpressive regime (Tannock et al., 2020a; 2020b). The footwall of this fault mainly consists of the Xinfengjiang pluton (the eastern portion of the Fogang batholith), a late Jurassic biotite granite that intruded into the basement of Proterozoic to Silurian age during the Yanshanian orogeny (Li et al., 2007; Tannock et al., 2020a; 2020b). Epidote veins are located in the mylonites at the transition between undeformed granite and fault zone (Tannock et al., 2020a). The hanging wall is composed of a quartz-sericite ultracataclasite/phyllonite in contact with a quartz reef and finally abutted by the sedimentary "Red Beds" of Cretaceous age (Tannock et al., 2020a). Since the epidote veins are either pre- or syn-kinematic with respect to the mylonites (Tannock et al., 2020b), we infer that the epidote veins cannot be older than the pluton itself, but they are also among the earliest structures related to the early movements of the Heyuan Fault (Tannock et al., 2020a; 2020b). Epidote veins are absent in the footwall cataclasite and in the quartz reef, which formed after the mylonite. Syn-kinematic epidote veins formed at a temperature of ca. 330 °C as indicated by the white mica composition in the mylonites (Tannock et al., 2020a). Sample Heyuan-1 is discussed in Tannock et al. (2020a; 2020b) and its sampling location is shown in Fig. 1 of Tannock et al. (2020a; their sample HY17-5).

3 Methods

Except where stated, sample preparation and measurements were carried out in the laboratory facilities of the Institute of Geological Sciences, University of Bern, Switzerland.

3.1 Imaging and screening methods for sample selection

Thin (30 μm) and thick (50–60 μm) sections were inspected by petrographic and electron microscopy, respectively on a ZEISS Axioplan microscope and on a ZEISS EVO50 SEM using BSE imaging (ca. 1 nA beam current, 20 kV accelerating voltage, working distance 8.5–10.0 mm). BSE images were used to plan analysis spots – all of the same size – within epidote grains so as to avoid mixing of different zonings in each single measurement, as well as mineral and fluid inclusions. Major element contents were acquired by electron probe micro-analyzer (EPMA), and REE, U, Th and Pb contents were measured by LA–ICP–MS upon screening many samples, employing methods presented elsewhere (Pettke et al., 2012). The details of the EPMA and LA–ICP–MS setups are reported in Appendix A.

3.2 U–Pb geochronology by LA–ICP–MS

Isotopic measurements of U, Th and Pb were performed on thin/thick sections for epidote and on acryl grain mounts for allanite. To minimize surface contamination, the thin/thick sections were cleaned with ethanol, and the grain mounts with ethanol and 5 % HNO_3. Measurements of U, Th and Pb isotopic ratios were performed with a Resonetics RESOlutionSE 193

nm excimer laser system (Applied Spectra, USA) equipped with a S-155 large-volume constant-geometry chamber (Laurin Technic, Australia) coupled with an Agilent 7900 ICP–QMS. The suitability of analytical conditions (Table 1) was checked in each session by performing preliminary analyses on secondary reference materials of known ages – namely CAP[b] allanite (for details see Burn et al., 2017), and CAP and AVC allanites (for details see Barth et al., 1994; Gregory et al., 2007) – and comparing them to their published U–Pb ages (see Table 2). Low fluence of 3 J s^{-2}, low repetition rate of 5 Hz and large spot size of 50 μm were combined to ensure a slow increase in depth/diameter ratio of the laser crater during a 40 sec ablation time, hence to minimize elemental (U/Th/Pb) DF. An additional session was carried out with a laser spot of 30 μm and the same laser conditions. The aim was to assess the effects of using a smaller spot size on the correction for DF (see Chew et al., 2014) and to explore whether the use of allanite as primary reference material can still provide accurate data at these conditions. If so, this would extend the applicability of the present protocol to smaller epidote grains. For this test, we selected two samples: the one also used for solution ICP–MS measurements (sample Abula-1; see Sect. 3.3), and the one with the smallest averaged analytical errors on ^{238}U/^{206}Pb and ^{207}Pb/^{206}Pb ratios (sample Grimsel-1). The 30 μm analyses were done in the same areas and crystals analyzed in the previous sessions after polishing the thin/thick sections to remove the condensation blankets around the ablation craters.

In all sessions, Tara allanite (see Gregory et al., 2007; Smye et al., 2014) is chosen as primary reference material because it is the most homogenous allanite in terms of U–Th–Pb isotopes and the most promising reference material for U–Pb geochronology (Gregory et al., 2007; Smye et al., 2014; Burn et al., 2017; Liao et al., 2020). Tara allanite reference isotopic ratios and their uncertainties (Table 2) were calculated by averaging five of the six ID–TIMS measurements reported by Smye et al. (2014), excluding the measurement that yielded the youngest U–Pb age outside uncertainty. The analytical sequence involved measurements of the reference Tara allanite interspersed between 3–9 sample measurements including allanite secondary reference materials for quality control. Analysis spots in allanite were planned based on BSE images to avoid chemical and isotopic heterogeneity (i.e. mixing of zoning) within each single analysis, and inclusions (e.g. rare < 1 μm sized thorite; Smye et al., 2014). A few analyses were however intentionally placed on fluid inclusions and across zoning in sample Albula-1 to ascertain that these features would not compromise the use of this sample for solution ICP–MS (see Sects. 3.3 and 4.3).

Raw data were treated in the software Iolite (version 7.08) by the VisualAge_UcomPbine Data Reduction Scheme (Chew et al., 2014), and the correction for DF was carried out by selecting an exponential function. Iolite fits this function to model the measured DF on the analyses of the primary reference material, and then applies it to all unknown analyses to correct them for DF. The quality of signals and that of the correction for DF were considered to determine the validity of each measurement. Assessing the quality of signals implies inspection of the laser signal of each isotope across each measurement to discard – partially or entirely – those that are contaminated by impurities such as mineral or fluid inclusions, or that show isotopic heterogeneity during ablation. The accuracy of DF correction depends on the ablation behavior being the same between primary reference material and sample, and is assessed by the unknowns giving flat ^{206}Pb/^{238}U ratios across the ablation once corrected for DF. Although we do not apply an initial Pb correction for age calculation, correcting the time-

resolved DF-corrected ^{206}Pb/^{238}U ratios for initial Pb ensures that no sloping results from zoning in initial Pb contents, which can be prominent in minerals with high initial Pb contents. A ^{208}Pb-correction is therefore applied to each analysis of the epidote unknowns using initial ^{207}Pb/^{206}Pb and ^{208}Pb/^{206}Pb ratios obtained from preliminary Tera–Wasserburg diagrams. This and the subsequent normalization of the measured ratios based on the reference values of the primary reference material

230   ensure that the ^{238}U/^{206}Pb and ^{207}Pb/^{206}Pb ratios used in the Tera–Wasserburg diagrams are true values, and that the U–Pb age calculated with these ratios is accurate. Since the isotopic fractionation between ^{207}Pb and ^{206}Pb is negligible (e.g. Burn et al., 2017), we address the suitability of the DF correction based on allanite as primary reference material only on ^{206}Pb/^{238}U ratios. A ^{207}Pb-correction was applied to the primary reference material (i.e. Tara allanite) by the VisualAge_UcomPbine Data Reduction Scheme (DRS) before it was used for normalization (Chew et al., 2014) using an initial ^{207}Pb/^{206}Pb value of

235   0.866 ± 0.079 obtained from a Tera–Wasserburg diagram plotting five ID–TIMS analyses by Smye et al. (2014), since it has been shown that initial ^{207}Pb/^{206}Pb ratios of allanite can deviate from model values (e.g. Cenki-Tok et al., 2014). The uncertainties on the ^{238}U/^{206}Pb and ^{207}Pb/^{206}Pb ratios obtained from the VisualAge_UcomPbine DRS (Chew et al., 2014) include an overall propagated uncertainty coming from the reproducibility of the primary reference material. Isoplot 3.7.5 (Ludwig, 2012) was used for age calculations. Age determination of epidote samples and allanite secondary reference

240   materials relies on the Tera–Wasserburg approach (Tera and Wasserburg, 1972; Ludwig, 1998). Since the initial Pb isotopic composition of CAP, CAP^{b} and AVC allanite is known and consistent with a modeled two-stage evolution of initial Pb isotopic compositions (Barth et al., 1994; Gregory et al., 2007; Burn et al., 2017), we ensured better age precision by anchoring the Tera–Wasserburg regressions of these allanite samples to an initial ^{207}Pb/^{206}Pb ratio of 0.854 ± 0.015 (275 Ma; Stacey & Kramers, 1975) and calculated their weighted average ^{207}Pb-corrected ^{238}U/^{206}Pb ages using the same value.

245   Regression and weighted average ^{207}Pb-corrected ^{238}U/^{206}Pb ages of allanite secondary reference materials are summarized in Table 3, and their Tera–Wasserburg diagrams are presented in Fig. B1 (Appendix B).

3.3 Solution ICP–MS

Independent measurements of ^{238}U/^{206}Pb and ^{207}Pb/^{206}Pb ratios were performed on two epidote micro-separates to check their consistency with U–Pb isotopic data measured by LA–ICP–MS and hence the reliability of the latter data. The material was

250   separated from the epidote-quartz vein of sample Albula-1, which is the one with the lowest degree of deformation and largest epidote crystals (see Sect. 4.1). Clean and pure epidote grains were handpicked under a binocular microscope. The epidote separates were pre-cleaned with MilliQ^{TM} water. Based on LA–ICP–MS U and Pb concentration data, four sample aliquots – two from each epidote micro-separate and each corresponding to ca. 300 ng of total Pb – were weighed in acid-cleaned Teflon beakers and dissolved following the procedure of Nägler and Kamber (1996). Samples were leached with

255   aqua regia at 120 °C for two days. The leachate was transferred into a second pre-cleaned Teflon beaker. To ensure complete dissolution a concentrated HF:HNO$_3$ (3:1 by volume) was added to the supernatant, and the beakers were placed on a heating plate at 90 °C for two days. After drying, 2 ml of 6.4 M HCl were added, and the beakers were placed on a heating plate at

150 °C for two days. The same procedure was applied to standard AGV-2 (Weis et al., 2006) as well as to two blanks, and complete dissolution was achieved for all samples and standards. Finally, the samples were dissolved in 1 ml 0.5 M HNO_3.

260 To determine $^{238}U/^{206}Pb$ ratios, a 10 % aliquot of digested samples and standards was further diluted with 0.5 M HNO_3 up to a final volume of 10 ml. Two solutions with two different dilution factors were prepared from each sample aliquot and were analyzed on a 7700x AgilentTM quadrupole ICP–MS at the Department of Geography, University of Bern, Switzerland. Standard AGV-2 (Weis et al., 2006) was used to correct for instrumental fractionation and to check accuracy of measurements. Final sample concentrations of ^{206}Pb, ^{207}Pb and ^{238}U (for both dilution factors of each sample aliquot) and

265 their corresponding analytical uncertainties as relative standard deviations – solely based on counting statistics – were calculated by referring to a calibration curve based on three dilution factors of AGV-2 standard. The $^{238}U/^{206}Pb$ ratio and uncertainty as 2 SE of each sample aliquot were calculated with Isoplot 3.7.5 (Ludwig, 2012) as weighted average values between the $^{238}U/^{206}Pb$ ratios calculated from the measurements of both dilution factors, which were the same within uncertainty for all sample aliquots. The remaining sample material was dried and re-dissolved in 0.5 ml 1 M HNO_3 for Sr–Pb

270 column chemistry using a pre-cleaned Sr-spec^{TM} resin (Horwitz et al., 1992). After loading, the sample matrix was eluted from the column with 1.5 ml 1 M HNO_3 while Sr and Pb were retained on the column. The Sr and Pb fractions were eluted with 1 ml of 0.01 M HNO_3 and 8 ml of 0.01 M HCl respectively, following Villa (2009) and Quistini et al. (2017). After drying, the Pb fraction was dissolved and further diluted in 0.5 M HNO_3 for measurement of Pb isotopes on a Thermo Fisher Neptune Plus MC–ICP–MS. Measurements were carried out in dry plasma mode using a CETAC Aridus 2 desolvating

275 system. Thallium was added to samples and standards to correct for instrumental mass fractionation with repeated measurements of NIST SRM 981 to quantify the external reproducibility of the measurements (Villa, 2009); the measured Pb isotopic composition was indistinguishable from those reported by Rehkämper and Mezger (2000). The four pairs of isotopic ratios measured by solution ICP–MS are only compared to the Tera–Wasserburg diagram based on LA–ICP–MS data (50 μm spot size) and are not used to calculate an age because the statistical robustness of a regression based on only

280 four data points is limited.

4 Results

4.1 Petrography and U–Th–Pb contents of samples selected for U–Pb geochronology

Four samples were selected for this contribution mainly based on 1) size of epidote grains in order to use the largest laser beam possible for LA–ICP–MS and 2) U contents that are both as high and as variable as possible within the sample. Larger

285 laser beams maximize the precision of U–Pb geochronology measurements. High U contents ensure higher contents of uranogenic Pb isotopes and therefore improve the precision of U and Pb isotopic measurements; their variability contributes to a larger spread of the analyses in Tera–Wasserburg diagrams for well-constrained regressions. The studied samples have epidote components (X_{Epi}) between 0.52–0.98 (calculated as $Fe^{3+}/(Al + Fe^{3+} - 2)$; Cr < limit of detection) and ΣREE between 3.3–210 μg g^{-1}.

290   One sample from the Albula area, sample Albula-1, was selected for U–Pb geochronology. Two veins can be recognized (Fig. 1a), both crosscutting the host rock with sharp boundaries:

1) 2–3 cm wide epidote-quartz-plagioclase vein (Vein1). Epidote grains are elongated, with lengths between ca. 0.5 mm along the vein boundaries to ca. 1 cm towards the center of the vein, with an aspect ratio up to ca. 7:1. Fractures are common and grains are euhedral to subhedral. Quartz is fractured and plagioclase is limited to a ca. 2 mm wide portion along the vein

295   boundaries, associated with the smallest epidote grains. U contents of epidote range between 3.7–89 µg g^{-1} (Table 4). Th contents are 0.01–0.05 µg g^{-1} (19/25 measurements are below the limits of detection of 0.03–0.07 µg g^{-1} with a spot size of 24 µm and 0.003 µg g^{-1} with a 60 µm spot size). Pb contents are 3.9–62 µg g^{-1}, total Pb/U ratios 0.14–10 and µ values 7–510.

2) ca. 1 mm wide epidote-quartz-plagioclase vein (Vein2). Epidote grains range between a few µm to 2 mm in diameter, most being fractured and euhedral to subhedral. Epidote grains of ca. 1–2 mm in diameter are mantled by thin layers of µm-

300   sized anhedral epidote grains. Quartz subgrains resulting from recrystallization and plagioclase wrap the epidote grains. U contents of epidote are 26–140 µg g^{-1} (Table 4), and Th contents 0.67–14 µg g^{-1}. Pb contents range from 24–64 µg g^{-1}, Pb/U ratios from 0.46–1.7 and µ values from 43–160.

BSE images of epidote (Fig. 2a) reveal growth zoning and intra-grain veinlets resulting from interaction with a secondary fluid. Sample Albula-1 was selected for solution ICP–MS given the large size of epidote grains.

305   Sample Grimsel-1 (Fig. 1b) displays a folded epidote-quartz vein crosscutting a weakly deformed portion of the host rock. Epidote grains are generally prismatic and range between a few µm to ca. 2 mm in size. They are mostly subhedral to anhedral and cracked, and they form clusters with no preferential grain orientation. Quartz subgrains indicate dynamic recrystallization via subgrain rotation. Green biotite and rare chlorite are associated with the epidote-bearing vein. Epidote in BSE images (Fig. 2b) exhibits weak patchy zonation towards the rims and the presence of porosity. K-feldspar is recognized

310   within epidote cracks. U contents are 54–350 µg g^{-1} (Table 4), and Th contents are 0.04–4.9 µg g^{-1}. Pb contents range between 79–190 µg g^{-1}, with Pb/U ratios from 0.45–1.7 and µ values between 41–160.

Sample Grimsel-2 (Fig. 1c) consists of an epidote-quartz-biotite vein cutting through a weakly deformed sector of the host rock. The vein boundaries are sharp and non-linear. Euhedral to subhedral epidote grains are cracked by stretching-induced fracturing, with single fragments ranging from a few µm to ca. 3 mm in size. Epidote grains can be estimated to have had an

315   aspect ratio up to ca. 6:1 before fracturing. Quartz is recrystallized by subgrain rotation. Biotite grain sizes range between ca. 100–500 µm. BSE images (Fig. 2c) show that epidote exhibits regular growth zoning. Epidote contains 109–535 µg g^{-1} of U and 0.07–0.53 µg g^{-1} of Th (Table 4). Pb contents range from 51–97 µg g^{-1}, Pb/U ratios are 0.20–0.86 and µ values 83–510.

Sample Heyuan-1 (Fig. 1d) is characterized by an epidote-quartz-K-feldspar-chlorite assemblage that fills pockets cutting through the granite-forming minerals or interstitial among the magmatic minerals. The sample is crosscut by quartz ±

320   hematite veins (see Fig. 4c in Tannock et al., 2020b). Epidote is variably shaped, from elongated without preferential orientation to prismatic. Epidote ranges between tens of µm to ca. 2 mm in length and forms clusters of euhedral to anhedral crystals. Quartz associated with epidote is mostly recrystallized, as indicated by the presence of quartz subgrains. Some mm-sized quartz grains, however, display undulose extinction. Chlorite associated with epidote forms interstitial aggregates of

ca. 500–1000 µm in size. Growth zoning of epidote is recognized from BSE images (Fig. 2d) and K-feldspar is intertwined with smaller-sized epidote grains along the boundaries of larger ones, as well as with quartz filling epidote fractures. The measured U content of Heyuan-1 epidote is 2.6–34 µg g^{-1} (Table 4). Th contents range between 0.04–38 µg g^{-1}, with most analyses below 10 µg g^{-1}. Pb contents are 9.4–27 µg g^{-1}, Pb/U ratios range between 0.42–4.4 and µ values between 16–190.

In summary, among the four samples selected for U–Pb geochronology, measured U contents of epidote are highly variable (2.6–530 µg g^{-1}; n = 80; Table 4), and the intra-sample variability in U concentrations is ca. one order of magnitude (Fig. 3). Samples Albula-1 and Heyuan-1 both contain a few to tens of µg g^{-1} of U, whereas samples Grimsel-1 and Grimsel-2 have higher U contents of hundreds of µg g^{-1}. Thorium concentrations span four orders of magnitude (0.01–38 µg g^{-1}; n = 56). Samples with similar U concentrations display different Th contents, creating variability in Th/U ratios. Pb contents are 3.9–190 µg g^{-1}, and Pb/U ratios span between 0.14–10, each sample varying to different extents. With only 4/88 Th measurements above 10 µg g^{-1} (one in sample Albula-1 and three in sample Heyuan-1), Th–Pb geochronology is not viable. All epidote samples exhibit µ values well below 2000.

4.2 Testing Tara allanite as a reference material for epidote U–Pb geochronology

To assess the validity of allanite as primary reference material for epidote dating, we compared the DF correction of ^{206}Pb/^{238}U ratios over the ablation time using Tara allanite as reference for CAP[b] allanite (Burn et al., 2017) as matrix-matched (Fig. 4a), for Plesovice zircon (Sláma et al., 2008) as non-matrix-matched (Fig. 4b), and for epidote as closely matrix-matched (Fig 5). An accurate correction for DF produces flat time-resolved lines of DF-corrected ^{206}Pb/^{238}U ratios for unknowns: sloping or more complex shaped curves indicate either zoning in initial Pb contents or that the DF correction is not compensating for the difference in matrix. As expected, CAP[b] allanite has DF-corrected ^{206}Pb/^{238}U ratios that are flat when standardized to Tara allanite (Fig. 4a, both measured with a 50 µm spot). Some of the DF-corrected ^{238}U/^{206}Pb ratios measured in Albula-1 and Grimsel-1 epidotes did not display a flat trend, and we therefore applied a ^{208}Pb correction to verify if this was due to zoning in initial Pb contents. The fact that the majority (122 out of 127 analyses) of ^{208}Pb- and DF-corrected time-resolved ^{206}Pb/^{238}U ratios are flat (Fig. 5) indicates similar ablation behavior and downhole fractionation of U from Pb between epidote and allanite for our analytical setup, and accurate correction for DF in epidote by using Tara allanite as primary reference material with both 50 µm (Fig. 5a-d) and 30 µm (Fig. 5e-f) spot sizes. The analyses whose ^{208}Pb- and DF-corrected time-resolved ^{206}Pb/^{238}U ratios are not flat or do not overlap with all other analyses were excluded from age calculation (see Sect. 4.3) as they could indicate either analytical instability during ablation or a different initial Pb isotopic composition. In contrast, the distinct ablation behavior of (Plesovice) zircon is revealed by complex shaped DF-corrected ^{238}U/^{206}Pb ratios even with a 50 µm spot (Fig. 4b; also see Fig. 6 of Burn et al., 2017).

4.3 Laser ablation ICP–MS U–Pb data of unknown samples

Uncertainties on LA–ICP–MS ^{238}U/^{206}Pb and ^{207}Pb/^{206}Pb ratios are 2 standard errors (2 SE), and all age uncertainties calculated with Isoplot are 95 % confidence.

A total of twenty-two spot analyses were measured in sample Albula-1 with a 50 µm spot (Table 5). $^{238}U/^{206}Pb$ ratios are 0.535–33.2 with uncertainties of 2–4 %. $^{207}Pb/^{206}Pb$ ratios are 0.586–0.837 ± 0.8–2 % (Table 5). No analyses were excluded as all ^{208}Pb- and DF-corrected time-resolved $^{206}Pb/^{238}U$ ratios are flat and overlap (Fig. 5a). A Tera–Wasserburg regression based on all data points (Fig. 6a) yields an intercept age of 62.7 ± 3.0 Ma (MSWD = 1.6) with a $^{207}Pb/^{206}Pb$ intercept of

360   0.8334 ± 0.0043. The good spread of the data points along the regression line reflects variable fractions of initial Pb (f_{206} = 0.69–1.0; Table 5). The small MSWD value indicates that there is no resolvable age difference between the two veins at the stated analytical precision. In fact, if the analyses from the two veins are considered separately, the Tera–Wasserburg ages of Vein1 and Vein2 are 67.6 ± 5.0 Ma (n = 18) and 58.9 ± 3.8 Ma (n = 4), which overlap within uncertainty. The initial $^{207}Pb/^{206}Pb$ ratio of Albula-1 epidote indicated by the Tera-Wasserburg diagram is within uncertainty of the model value of

365   0.840 ± 0.015 at 63 Ma (Stacey & Kramers, 1975). By using this model initial ratio for a ^{207}Pb-correction, the weighted average ^{207}Pb-corrected $^{238}U/^{206}Pb$ age is 65.0 ± 2.5 Ma (MSWD = 0.91). Eighteen additional measurements were carried out in sample Albula-1 (10 in Vein1 and eight in Vein2) with a spot size of 30 µm. Analysis 8 (Table 5) was excluded from age calculation because it was considered unreliable based on its ^{208}Pb- and DF-corrected time-resolved $^{206}Pb/^{238}U$ ratio (Fig. 5e). The Tera–Wasserburg diagram based on 17 analyses with a 30 µm spot yields an intercept age of 65.9 ± 4.6 Ma and a

370    $^{207}Pb/^{206}Pb$ intercept of 0.8308 ± 0.0087 (MSWD = 1.4). Both values are within uncertainty of those obtained with a spot size of 50 µm. By combining the 50 and 30 µm datasets, an intercept age of 63.9 ± 2.6 Ma is obtained with an initial $^{207}Pb/^{206}Pb$ ratio of 0.8331 ± 0.0039 (MSWD = 1.6). Given the consistency of the measured U–Pb data (i.e. no isotopic heterogeneity given by fluid inclusions and zonation even with different spot sizes), sample Albula-1 is considered suitable for solution ICP–MS (see Sect. 4.4).

375   Twenty-three 50 µm analyses were carried out in sample Grimsel-1. Analysis 14 (Table 5) was excluded as its ^{208}Pb- and DF-corrected time-resolved $^{206}Pb/^{238}U$ ratio does not overlap with all other analyses (Fig. 5b), possibly indicating a different initial Pb isotopic composition. Twenty-two analyses define a regression in a Tera–Wasserburg diagram (Fig. 6b) with an intercept age of 19.2 ± 4.3 Ma (MSWD = 0.79) and a $^{207}Pb/^{206}Pb$ intercept of 0.7964 ± 0.0027. All data points plot close to the y-axis ($^{238}U/^{206}Pb$ ratios = 1.10–10.3 ± 2–4 %; $^{207}Pb/^{206}Pb$ ratios = 0.774–0.794 ± 0.5–0.8 %; Table 5), indicating high

380   and nearly invariable initial Pb fractions (f_{206} = 0.97–1.0; Table 5) in all measurements. The initial $^{207}Pb/^{206}Pb$ value is outside uncertainty of the model initial $^{207}Pb/^{206}Pb$ ratio of 0.837 ± 0.015 at 19 Ma of Stacey and Kramers (1975). Hence, a ^{207}Pb-correction with the modeled ratio would yield an inaccurate weighted average ^{207}Pb-corrected $^{238}U/^{206}Pb$ age; thus this sample can only be dated by the Tera–Wasserburg approach. Twenty-five additional measurements were made with a spot size of 30 µm. Analysis 13 (Table 5) is excluded based on its ^{208}Pb- and DF-corrected time-resolved $^{206}Pb/^{238}U$ ratio not

385   overlapping with the other analyses (Fig. 5f). The Tera–Wasserburg age based on 22 analyses is 17 ± 10 Ma with MSWD of 1.3. The initial $^{207}Pb/^{206}Pb$ of 0.7863 ± 0.0049 is slightly outside uncertainty of that obtained with a spot size of 50 µm. The age obtained by combining the analyses with 50 and 30 µm spot sizes is 15.2 ± 6.5 Ma with an initial $^{207}Pb/^{206}Pb$ ratio of 0.7918 ± 0.0037. However, MSWD of the combined dataset is 2.6, much higher than those obtained from the analyses with constant spot size, indicating that the two datasets should be treated separately.

Sixteen 50 μm analyses of sample Grimsel-2 define a regression in the Tera–Wasserburg diagram (Fig. 6c) yielding an age of 16.9 ± 3.7 Ma (MSWD = 0.40). No analyses were excluded before age calculation (Fig. 5c). The spread along the regression is limited and the data points are close to the y-axis (^{238}U/^{206}Pb ratios = 8.35–20.1 ± 2–3 %; ^{207}Pb/^{206}Pb ratios = 0.759–0.784 ± 0.7–0.9 %; Table 5), indicating high and similar fractions of initial Pb in all analyses (f_{206} = 0.95–0.98; Table 5). The initial ^{207}Pb/^{206}Pb ratio of 0.7998 ± 0.0054 is outside uncertainty of the model initial ^{207}Pb/^{206}Pb value of 0.837 ± 0.015 at 17 Ma (Stacey and Kramers, 1975), which cannot be used for a ^{207}Pb-correction. The Tera–Wasserburg approach is therefore the only viable to date this sample.

Twenty-three analyses were carried out in sample Heyuan-1 with a spot size of 50 μm, and analyses 22 and 23 (Table 5) were excluded based on the anomalous ^{208}Pb- and DF-corrected time-resolved ^{206}Pb/^{238}U ratios (Fig. 5d). Twenty-one analyses define a regression (Fig. 6d) with an age of 107.2 ± 8.9 Ma (MSWD = 0.91). Initial Pb fractions are highly variable in the different measurements (f_{206} = 0.71–0.99; Table 5) yielding appreciable spread along the regression (^{238}U/^{206}Pb ratios = 0.753–18.2 ± 3–4 %; ^{207}Pb/^{206}Pb ratios = 0.596–0.809 ± 2–3 %; Table 5). The initial ^{207}Pb/^{206}Pb ratio of 0.8161 ± 0.0061 indicated by the upper intercept is outside uncertainty of the modeled initial ^{207}Pb/^{206}Pb value of 0.843 ± 0.015 at 107 Ma (Stacey and Kramers, 1975). Thus, the age of this sample is best determined from the Tera-Wasserburg regression.

On a final note, we have calculated Tera–Wasserburg regression ages of the presented epidote samples by using a different primary reference material: CAP[b] (June 2019; reference values from Burn et al., 2017) and CAP (July 2019 and January 2020; reference values from Barth et al., 1994) allanite. The resulting epidote U–Pb ages remain within uncertainty identical to those calculated with Tara allanite as primary reference material (Appendix C).

4.4 Solution ICP–MS U–Pb data

Uncertainties on solution ICP–MS ^{238}U/^{206}Pb and ^{207}Pb/^{206}Pb ratios are 2 standard errors (2 SE).

For measurements by solution ICP–MS of ^{238}U/^{206}Pb and ^{207}Pb/^{206}Pb ratios in Albula-1 epidote, ca. 30 mg of material were necessary to ensure ca. 300 ng of total Pb. ^{238}U/^{206}Pb ratios range between 3.04–3.67 with uncertainties between 0.8–1.6 %, and ^{207}Pb/^{206}Pb ratios between 0.81319–0.81674 ± 0.03–0.04 ‰ (Table 6). The uncertainties on solution ICP–MS ^{238}U/^{206}Pb ratios are lower than those measured by LA–ICP–MS with a 50 μm spot size by a factor of 2.5, and a decrease by a factor of 13–100 occurs in analytical uncertainties on ^{207}Pb/^{206}Pb ratios. The two aliquots from each epidote micro-separate (A–B and C–D in Table 6) yield identical ratios within uncertainty. ^{238}U/^{206}Pb and ^{207}Pb/^{206}Pb ratios display minor spread in a Tera–Wasserburg diagram (Fig. 7). In comparison to LA–ICP–MS data, the intra-sample variability of the solution ICP–MS ^{238}U/^{206}Pb and ^{207}Pb/^{206}Pb ratios is only 2 % and 14 % respectively, attesting to homogenization of initial Pb fractions in the micro-separates. This confirms that no statistically robust Tera-Wasserburg regression can be calculated from the solution ICP–MS data alone. The ^{238}U/^{206}Pb and ^{207}Pb/^{206}Pb ratios measured by solution ICP–MS overlap with individual LA–ICP–MS data points (50 μm spot; Fig. 7).

5 Discussion

5.1 CAP[b], CAP and AVC allanite as quality control

Although allanite geochronology is beyond the scope of this contribution, analyses of CAP[b], CAP and AVC allanite provide a quality control on U–Pb measurements during the analytical sessions. The epidote samples analyzed in this study contain too little Th for Th–Pb geochronology and we only explore epidote as a U–Pb geochronometer. For this reason, although the usual reference ages for allanite are Th–Pb ages, we check the reliability of our U–Pb measurements of allanite secondary reference materials by comparing them to published U–Pb ages (see Table 2) rather than their Th–Pb reference ages. In fact, ages from the two systems differ for these allanite samples likely due to excess ^{206}Pb and open-system behavior of the U–Pb system as opposed to the Th–Pb one (Barth et al., 1994; Oberli et al., 2004; Gregory et al., 2007; 2012; Darling et al., 2012; El Korh, 2014; Smye et al., 2014; Burn et al., 2017). Although this is a relevant issue in allanite geochronology per se, it does not impact the usefulness of allanite as secondary reference material for U–Pb dating in that it is the reproducibility of measured U–Pb ages in comparison with published values that confirms the reliability of U–Pb measurements. Tera–Wasserburg and weighted average ^{207}Pb-corrected ^{238}U/^{206}Pb ages determined from our analyses of CAP[b], CAP and AVC allanite (Table 3) in all analytical sessions are overall consistent with their published U–Pb ages, attesting to the reliability of our U–Pb measurements. AVC allanite analyzed in two sessions provided Tera–Wasserburg ages of 292.4 ± 3.7 Ma and 285.2 ± 4.5 Ma and identical weighted average ^{207}Pb-corrected ^{238}U/^{206}Pb ages. Our AVC allanite ages are within uncertainty of the Tera–Wasserburg age of 289.6 ± 5.6 Ma of Gregory et al. (2007). CAP[b] allanite (Burn et al., 2017) was used in one session, yielding a Tera–Wasserburg age of 284.2 ± 2.6 Ma and a weighted average ^{207}Pb-corrected ^{238}U/^{206}Pb age of 284.2 ± 2.0 Ma, both within uncertainty of those calculated by Burn et al. (2017) of respectively 284.9 ± 2.8 Ma and 283.8 ± 2.8 Ma. CAP allanite was used in two sessions returning intercept ages of 288.5 ± 2.9 Ma and 283.0 ± 3.4 Ma, with comparable weighted average ^{207}Pb-corrected ^{238}U/^{206}Pb ages. Our CAP U–Pb ages are within uncertainty of or close to the U–Pb age of 275.0 ± 4.7 Ma determined by SHRIMP by Gregory et al. (2007). The ages of CAP[b], CAP and AVC allanite obtained from unanchored Tera-Wasserburg regressions through our data are identical to those obtained from the anchored regressions but less precise (Table 3). We acknowledge that the Tera–Wasserburg age of 288.5 ± 2.9 Ma obtained from CAP allanite in the July 2019 session is slightly outside uncertainty of that reported by Gregory et al. (2007). However, we do not regard this difference outside uncertainty of ca. 2 % as significant given the complications of U–Pb age determinations of CAP allanite (e.g. Barth et al., 1994; Burn et al., 2017), and given the fact that AVC allanite used in the same session yielded an age within uncertainty of that measured by Gregory et al. (2007), attesting to reliable U–Pb measurements.

The values of excess variance calculated by Isoplot 3.7.5 (Ludwig, 2012) from the ^{207}Pb-corrected ages of CAP and AVC allanite samples in all analytical sessions conducted between July 2019 and October 2020 are respectively 1.9 and 2.2 % (2σ). These values are considered reasonable estimates of the long-term reproducibility, but they are not propagated onto our epidote ages because 1) they are not directly applicable to Tera–Wasserburg regression ages and 2) the effect of the propagation would be negligible.

5.2 Tara allanite as reference material for LA–ICP–MS dating of epidote

455 The presented data confirm that Tara allanite is an appropriate primary reference material for U–Pb dating of epidote by LA–ICP–MS in spot-analysis mode. The primary reference material is used to correct the measured isotopic ratios for DF, which is crucial to obtain reliable U–Pb geochronology by LA–ICP–MS (Horstwood et al., 2016). In this respect, 122 out of 127 analyses of epidote yield ^{208}Pb- and DF-corrected ^{206}Pb/^{238}U ratios that are flat and that overlap throughout ablation time, demonstrating that the correction for DF is accurately carried out by using Tara allanite with a spot size of 50 μm and even

460 30 μm (Fig. 5). This is corroborated by the fact that the Tera–Wasserburg ages and initial ^{207}Pb/^{206}Pb ratios of Albula-1 and Grimsel-1 epidotes with a 30 μm spot remain consistent with the dataset with a 50 μm spot size. However, in both epidote samples age precision decreases with a spot of 30 μm. In the case of Grimsel-1 epidote, this is expected because the poor spread in ^{238}U/^{206}Pb and ^{207}Pb/^{206}Pb ratios, combined with larger analytical uncertainties of the 30 μm measurements, leads to an even more poorly constrained regression than that with a 50 μm spot size. Thanks to the larger spread in plotted ratios of

465 Albula-1 epidote, the effects of the lower analytical precision with a 30 μm spot size are less dramatic but still noticeable. The flat and overlapping trends of most ^{208}Pb- and DF-corrected time-resolved ^{206}Pb/^{238}U ratios of sample Grimsel-1 (Fig. 5b and f) indicate that the fact that its initial ^{207}Pb/^{206}Pb ratios are slightly outside uncertainty when measured with different spot sizes cannot be due to inaccurate correction for DF.

5.3 Validation of ^{238}U/^{206}Pb and ^{207}Pb/^{206}Pb ratios by solution ICP–MS and considerations on analyzed volumes versus
470 **age precision**

The consistency between the datasets acquired by different techniques lends support to the accuracy of our LA–ICP–MS data and of the calculated Tera–Wasserburg ages. The minor variability of ^{238}U/^{206}Pb ratios measured by solution ICP–MS data despite the high analytical precision with respect to LA–ICP–MS acquisitions is expected because sample preparation for solution ICP–MS requires homogenization of ca. 9×10^9 μm^3 (ca. 30 mg of material). By comparison, with LA–ICP–MS

475 homogenization occurred over a volume of ca. $20–24 \times 10^3$ μm^3, as the measured depth of the LA–ICP–MS craters is between 10–12 μm. With decreasing spread in the plotted LA–ICP–MS ^{238}U/^{206}Pb and ^{207}Pb/^{206}Pb ratios, the regression becomes less constrained. Epidote samples Grimsel-1 and Grimsel-2 give larger uncertainties than Albula-1 and Heyuan-1 epidote because of the more limited spread in their LA–ICP–MS data points despite having higher U and Pb contents and hence better counting statistics. This suggests that higher analytical precision alone does not ensure better age precision unless it is

480 accompanied by a large-enough data-point spread on the Tera Wasserburg diagram. It also confirms that epidote samples with relatively low U and Pb contents should not be automatically considered unsuitable for U–Pb geochronology.

It is therefore crucial that the spot size of LA–ICP–MS analyses represent a compromise ensuring sufficient analytical precision and the smallest extent possible of sample homogenization in order to preserve the variability in initial Pb contents. It should be noted that the analyzed samples are characterized by variable Th/U ratios (Fig. 3). The fractionation of Th from

485 U is commonly attributed to oxidizing conditions (e.g. Frei et al., 2004). It is thus possible that the variability in initial Pb

fractions of each individual epidote vein might be determined by physico-chemical conditions upon epidote crystallization, such as oxidizing conditions or re-equilibration along fluid pathways.

5.4 Isotopic composition of initial Pb

Among the epidote samples analyzed in this study, only Albula-1 epidote gives an initial ^{207}Pb/^{206}Pb ratio that overlaps within uncertainty with the model value of Stacey & Kramers (1975). Accordingly, the weighted average ^{207}Pb-corrected ^{238}U/^{206}Pb age of sample Albula-1 is within uncertainty of its Tera–Wasserburg age. Epidotes from all other samples yielded Tera–Wasserburg initial ^{207}Pb/^{206}Pb ratios that deviate from model values, indicating non-negligible additions of inherited radiogenic components to the initial Pb. Radiogenic Pb components can be inherited by the fluid at its source and/or during circulation and re-equilibration with rocks along its pathway containing U-Th-bearing minerals (e.g. Romer, 2001). The weighted average ^{207}Pb-corrected ^{238}U/^{206}Pb ages of epidote Grimsel-1, Grimsel-2 and Heyuan-1 calculated by assuming a model initial ^{207}Pb/^{206}Pb ratio would be grossly inaccurate, implying that these three samples can only be dated with a Tera–Wasserburg regression. These considerations confirm the Tera–Wasserburg approach as the most suitable – and often the only viable – for accurate U–Pb dating of low-μ phases such as epidote (see Romer, 2001; Romer and Xiao, 2005; Odlum and Stockli, 2019; 2020).

5.5 Geological constraints on epidote U–Pb ages

To evaluate the geological accuracy of the U–Pb ages calculated from epidote in the veins presented above we consider other geochronological constraints on the deformation history of their respective host rocks. Albula-1 epidote gives a Paleocene age of 62.7 ± 3.0 Ma. Although, to our knowledge, no isotope geochronology is available in the Albula region, our epidote U–Pb age is consistent with geodynamic events taking place in its surroundings. For example, the Err–Platta system was investigated by Handy et al. (1996) and their D2 – in the stability field of epidote – is dated 80–67 Ma (K–Ar on white mica); epidote growth is also observed in the post-D2 deformation (Handy et al., 1996). A rutile U–Pb age of 63.0 ± 3.0 Ma was calculated by Picazo et al. (2019) from the Malenco–Margna boundary (Passo d'Ur, ca. 90 km south-southeast of the Albula area; Fig. 1a in Picazo et al., 2019) dating the stacking of the nappes associated with metamorphism at high pressure. Sample Grimsel-1 yielded initial ^{207}Pb/^{206}Pb ratios that differ outside uncertainty when measured with different spot sizes (50 vs. 30 μm). Although minimal, the difference in initial ^{207}Pb/^{206}Pb ratios given by the 50 and 30 μm measurements might indicate isotopic heterogeneity or unreliability of the 30 μm dataset. The 30 μm analyses were carried out in the same epidote grains as the 50 μm ones and no textural evidence (e.g. zoning) supports isotopic heterogeneity. Therefore, we regard the 30 μm dataset as questionable from a technical standpoint and only discuss the results obtained from the 50 μm dataset. Epidote U–Pb ages in samples Grimsel-1 and Grimsel-2 yield (early) Miocene ages of 19.2 ± 4.3 Ma and 16.9 ± 3.7 Ma respectively. These ages are within uncertainty of each other and can be attributed to the early deformation in the area between 22–17 Ma (Handegg phase; Challandes et al., 2008; Rolland et al., 2009). This is corroborated by the presence of green biotite associated with epidote in the epidote-bearing veins (Challandes et al., 2008; Rolland et al., 2009; Herwegh et

al., 2017; Wehrens et al., 2017). Notably, Grimsel-1 and Grimsel-2 epidote samples yield initial $^{207}Pb/^{206}Pb$ ratios that are identical within uncertainty and indicate an inherited radiogenic component. This implies that the Pb isotopic signature of the circulating fluid(s) was homogenously re-equilibrated over a ca. 100 m distance.

Epidote of sample Heyuan-1 yields an age of 107.2 ± 8.9 Ma, which is (early) Cretaceous and consistent with the earliest movements of the Heyuan Fault. This is supported by the sample being crosscut by an earliest-generation quartz vein associated with hematite, as the formation of quartz veins post-dates that of epidote veins across the Heyuan fault but is related to the early phases of faulting (Tannock et al., 2020a; 2020b).

5.6 Epidote ages as time of crystallization in low-temperature veins

Having established that the calculated epidote U–Pb ages are consistent with geological events that affected the host rocks, we now discuss whether these ages can be truly considered representative of epidote crystallization. The highest temperatures recorded by the deformation events that affected the meta-granitoid rocks hosting the analyzed epidote veins at Albula Pass, at Grimsel Pass and at the Heyuan Fault are respectively 300 °C (Mohn et al., 2011), 450 ± 30 °C (Challandes et al., 2008; Goncalves et al., 2012) and 330 °C (Tannock et al., 2020a). All these temperatures are well below 685–750 °C, proposed by Dahl (1997) as the range for the closure temperature of Pb diffusion in epidote. Nevertheless, resetting of the U–Pb geochronometer can occur independently of temperature-controlled diffusion via fluid-mediated dissolution–precipitation processes, which can be assessed with BSE imaging. Albula-1 and Grimsel-2 epidotes display growth zoning, which is regarded as primary zoning and thus lack of significant elemental diffusion (Franz and Liebscher, 2004). Since care was taken to avoid mixing of different zoning domains in each single analysis – including those associated with secondary veinlets – and considering that the MSWDs of the calculated epidote ages are all close to or below 1 (i.e. only one epidote generation can be distinguished at the stated analytical precision), we can conclude that the ages of Albula-1 and Grimsel-2 epidote date their crystallization and therefore the formation of the epidote-bearing veins.

The epidote-bearing vein in sample Grimsel-1 is folded; epidote does not display prominent zoning, and it is fractured and porous. This may raise questions as to whether the age of 19.2 ± 4.3 Ma dates the formation of Grimsel-1 epidote or the resetting of the U–Pb geochronometer by interaction with a fluid assisting the Alpine deformation. However, epidote is associated with green biotite, hinting that the vein epidote formed during the Handegg phase (22–17 Ma) in the stability field of green biotite (Challandes et al., 2008; Rolland et al., 2009; Herwegh et al., 2017; Wehrens et al., 2017). Therefore, the age of 19.2 ± 4.3 Ma is interpreted as the crystallization age of epidote. The minor presence of chlorite may indicate that the subsequent folding of the vein may have occurred at the end of the Handegg phase or at the beginning of the Oberaar phase with the onset of chlorite crystallization (Herwegh et al., 2017; Wehrens et al., 2017).

In sample Heyuan-1, epidote is present in pockets filled by an epidote-quartz(-chlorite) assemblage. This microstructure might suggest a magmatic origin of epidote, and consequently that epidote might have formed in the Jurassic as a magmatic mineral and that the U–Pb system was reset by ingression of fluids related to the first movements of the Heyuan Fault. However, a magmatic origin of the epidote can be ruled out based on the association of epidote with chlorite instead of

biotite (the magmatic phyllosilicate stable in the Xinfengjiang pluton; Li et al., 2007; Tannock et al., 2020a; 2020b) Coexistence with chlorite is consistent with the temperature of mylonitization during Heyuan normal faulting (330 °C; Tannock et al., 2020a). Furthermore, the Th/U ratios measured in Heyuan-1 epidote are << 1, whereas the Fogang Batholith – which comprises the Xinfengjiang pluton – has Th/U ratios >> 1 (Li et al., 2007). This lands support to a non-magmatic origin of the studied epidote because epidote generally reflects the trace element composition of its host rock (Frei et al., 2004). We thus conclude that all epidote U–Pb ages presented in this study date the crystallization of the epidote grains that formed during low-temperature fluid circulation.

6 Concluding remarks and future prospects

This contribution presents a protocol to determine U–Pb ages and initial $^{207}Pb/^{206}Pb$ compositions of epidote (i.e. epidote–clinozoisite solid solution), that is highly but variably enriched in initial Pb. This includes preliminary screening of the material to verify the presence of sufficiently high U contents (mainly between 7–310 µg g^{-1} in our samples) and intra-sample chemical variability. If these geochemical characteristics are ascertained, measurements by spot-analysis LA–ICP–MS using a quadrupole mass spectrometer can allow U–Pb ages to be determined with uncertainties between ca. 5–20 %, the lowest precision being related to poor variability in initial Pb fractions. It is demonstrated that epidote and allanite have similar downhole fractionation of Pb from U during LA–ICP–MS spot analysis, and the consistency between the data measured by LA–ICP–MS and solution ICP–MS corroborates the accuracy of $^{238}U/^{206}Pb$ and $^{207}Pb/^{206}Pb$ ratios for epidote samples determined by using Tara allanite as primary reference material. We have shown that all effects due to downhole fractionation are accurately corrected for even with a spot size as small as 30 µm by using Tara allanite as primary reference material. Therefore, the lack of a standard that is perfectly matrix-matched to epidote does not prevent U–Pb dating of the epidote–clinozoisite solid solution by spot-analysis LA–ICP–MS with precision between ca. 5–20 %. The geological significance of the ages is verified against the geological evolution of the areas of origin of the epidote samples. In each sample, the obtained ages are interpreted as dating epidote crystallization during hydrothermal-vein formation.

The key strategy for U–Pb dating of epidote is the Tera–Wasserburg regression through data uncorrected for initial Pb. U–Pb geochronology of epidote is most successful when the epidote samples display large-enough variability in initial Pb fractions – even when high analytical precision is achieved – which may be related to variable physico-chemical conditions during the crystallization of vein-filling epidote. Although it is recommended that the largest spot size possible be used to ensure good counting statistics, it is imperative that geochemical heterogeneity be preserved among the different analyses in order to obtain a well-constrained Tera–Wasserburg regression and a small age uncertainty. An unexpected perk highlighted by the present study is that relatively low U contents (i.e. tens of µg g^{-1}) do not necessarily hamper age determinations at a geologically useful precision provided that the spread of $^{238}U/^{206}Pb$ and $^{207}Pb/^{206}Pb$ ratios is large enough.

This study presents a protocol that can be readily applied to date epidote-bearing hydrothermal veins and to assess initial Pb isotopic variability of the epidote-forming fluid. Better insight can now be gained from the application of epidote U–Pb

dating into the mechanisms that led to the hydration of the continental crust in the Aar Massif and in the Err nappe. This study represents the base from which further developments may allow to date high-P epidote-bearing veins in subducted oceanic units and to determine at the same time where the vein-forming fluid originated thanks to the combination of trace element, age and isotopic data measured in epidote. Multiple phases of fault re-activation may be identified in fault-plane epidote. Whether or not plagioclase recrystallization in metamorphosed granitoid rocks is linked to the formation of epidote-bearing veins may be solved by measuring U–Pb ages and initial Pb isotopic compositions in epidote, which has proven its potential to become an invaluable geochemical, isotopic and geochronological tool.

Appendix A

Contents of major elements were measured by electron probe micro-analyzer (EPMA) using a JEOL-8200 microprobe at the Institute of Geological Sciences (University of Bern) with 15 KeV accelerating voltage, 10 nA specimen current and 2 μm electron beam diameter. The following natural and synthetic standards were used for calibration: wollastonite (SiO_2), olivine (MgO), anorthite (CaO, Al_2O_3), garnet (FeO), Topaz (F), tephroite (MnO), tugtupite (Cl), rutile (TiO_2) and celestite (SrO). Structural formula was calculated based on 12.5 oxygen cations.

REE, U, Th and Pb contents of epidote samples were measured on thin (30 μm) or thick (50–60 μm) sections, pre-cleaned with ethanol. Concentrations in sample Albula-1 were measured on a Geolas Pro 193 nm ArF excimer laser (Coherent, USA) coupled with an ELAN DRCe quadrupole ICP–MS (QMS; Perkin Elmer, USA) at the Institute of Geological Sciences (University of Bern). Instrument optimization and measurement procedures [similar to those reported in Pettke et al. (2012)] employed an ablation rate of ca. 0.1 μm per laser pulse, 10 Hz, and beam sizes between 24 and 60 μm, the largest possible to minimize limits of detection and to avoid inclusions and fractures. Ablation was done in a 1 l min^{-1} He-0.008 l min^{-1} H_2 atmosphere. Concentrations in samples Grimsel-1, Grimsel-2 and Heyuan-1 were measured on a RESOlutionSE 193 nm excimer laser system (Applied Spectra, USA) equipped with a S-155 large-volume constant-geometry chamber (Laurin Technic, Australia) coupled with an Agilent 7900 ICP–QMS. Ablation was carried out in He atmosphere, which was allowed to mix with Ar carrier gas for transport to the ICP–MS. Repetition rate was 5 Hz, at spot sizes between 20 and 50 μm.

On both systems, analytical conditions were optimized on NIST SRM612 so as to keep ThO production rate < 0.2 % and Th/U sensitivity ratio of 0.97–1.0, the latter indicative of robust plasma conditions. GSD-1G from USGS was employed as the external standard whereas quality control was monitored by measuring SRM612 from NIST measured as an unknown. A true-time linear drift correction was applied by bracketing standardization. Data acquired on both systems were reduced off-line using SILLS (Guillong et al., 2008), with the sum of measured total oxides (98.3 % for epidote and 100 % for SRM-NIST 612) used for internal standardization (compare Halter et al., 2002). Limits of detection were rigorously calculated for each element in each analysis employing the formulation detailed in Pettke et al. (2012).

Appendix B

Tera–Wasserburg diagrams of allanite secondary reference materials. All regressions are anchored to a $^{207}Pb/^{206}Pb$ intercept of 0.854 ± 0.015 at 275 Ma following Stacey and Kramers (1975) and all age uncertainties are 95 % confidence.

Appendix C

Author contribution

Veronica Peverelli prepared the samples, ran the measurements, reduced and evaluated the data, and prepared the manuscript. Tanya Ewing, Daniela Rubatto, Alfons Berger and Marco Herwegh laid out the project. Martin Wille and Igor Maria Villa supervised the work in the clean lab for digestion of epidote micro-separates, as well as the measurements and data reduction of solution ICP–MS data. Pierre Lanari helped with the EPMA measurements, contributed to the discussions on the analytical LA–ICP–MS setup, and provided fundamental insight into LA–ICP–MS data evaluation and processing. Thomas Pettke enabled the measurements of REE, Pb, Th and U contents by LA–ICP–MS. Alfons Berger and Marco Herwegh helped with the geological interpretation of the data. All authors were involved in data evaluation and interpretation, and in the writing of the manuscript.

Acknowledgements

The authors thank Elizabeth Catlos, James Darling and Axel Schmitt for their constructive reviews and suggestions. Veronica Peverelli would like to thank Francesca Piccoli, Gabriela Baltzer and Daniel Rufer for the help in the laboratories, Lisa Tannock for providing samples and Patrick Neuhaus from the Geography Department of University of Bern for carrying out the solution ICP–MS measurements of $^{238}U/^{206}Pb$ ratios. We acknowledge funding of our new LA–ICP–MS facility through Swiss National Science Foundation, project 206021_170722, to Daniela Rubatto and Thomas Pettke. The solution ICP–MS isotope data was obtained on a Neptune MC–ICP mass spectrometer acquired with funds from the NCCR PlanetS supported by the Swiss National Science Foundation grant nr. 51NF40-141881. This work is part of the PhD thesis of Veronica Peverelli, who acknowledges SNF funding (project nr. 178785) granted to Alfons Berger.

Competing interests

The authors declare that they have no conflict of interest.

Code/data availability

All data are included in the manuscript (see tables).

References

640 Barker, S. L. L., Cox, S. F., Eggins, S. M. and Gagan, M. K.: Microchemical evidence for episodic growth of antitaxial veins during fracture-controlled fluid flow, Earth Planet. Sci. Lett., 250(1–2), 331–344, doi:10.1016/j.epsl.2006.07.051, 2006.

Barker, S. L. L., Bennett, V. C., Cox, S. F., Norman, M. D. and Gagan, M. K.: Sm-Nd, Sr, C and O isotope systematics in hydrothermal calcite-fluorite veins: Implications for fluid-rock reaction and geochronology, Chem. Geol., 268(1–2), 58–66, doi:10.1016/j.chemgeo.2009.07.009, 2009.

645 Barth, S., Oberli, F. and Meier, M.: Th-Pb versus U-Pb isotope systematics in allanite from co-genetic rhyolite and granodiorite: implications for geochronology, Earth Planet. Sci. Lett., 124(1–4), 149–159, doi:10.1016/0012-821X(94)00073-5, 1994.

Berger, A., Mercolli, I., Herwegh, M., Gnos, E.: Geological Map of the Aar Massif, Tavetsch and Gotthard Nappes. – Geol. spec. Map 1:100 000, explanatory notes 129, Federal Office of Topography swisstopo, 2017.

650 Bird, D.K., Spieler, A.R.: Epidote in Geothermal Systems, Rev. Mineral. Geochemistry 56, 235–300, https://doi.org/10.2138/gsrmg.56.1.235, 2004.

Bons, P. D., Elburg, M. A. and Gomez-Rivas, E.: A review of the formation of tectonic veins and their microstructures, J. Struct. Geol., 43, 33–62, doi:10.1016/j.jsg.2012.07.005, 2012.

Buick, I. S., Frei, R. and Cartwright, I.: The timing of high-temperature retrogression in the Reynolds Range, central

655 Australia: Constraints from garnet and epidote Pb-Pb dating, Contrib. to Mineral. Petrol., 135(2–3), 244–254, doi:10.1007/s004100050510, 1999.

Burn, M., Lanari, P., Pettke, T. and Engi, M.: Non-matrix-matched standardisation in LA-ICP-MS analysis: General approach, and application to allanite Th-U-Pb dating, J. Anal. At. Spectrom., 32(7), 1359–1377, doi:10.1039/c7ja00095b, 2017.

660 Catlos, E. J., Sorensen, S. S. and Harrison, T. M.: Th-Pb ion-microprobe dating of allanite, Am. Mineral., 85(5–6), 633–648, doi:10.2138/am-2000-5-601, 2000.

Cenki-Tok, B., Darling, J. R., Rolland, Y., Dhuime, B. and Storey, C. D.: Direct dating of mid-crustal shear zones with synkinematic allanite: New in situ U-Th-Pb geochronological approaches applied to the Mont Blanc massif, Terra Nov., 26(1), 29–37, doi:10.1111/ter.12066, 2014.

665 Challandes, N., Marquer, D. and Villa, I. M.: P-T-t modelling, fluid circulation, and 39Ar-40Ar and Rb-Sr mica ages in the Aar Massif shear zones (Swiss Alps), Swiss J. Geosci., 101(2), 269–288, doi:10.1007/s00015-008-1260-6, 2008.

Chew, D. M., Petrus, J. A. and Kamber, B. S.: U-Pb LA-ICPMS dating using accessory mineral standards with variable common Pb, Chem. Geol., 363, 185–199, doi:10.1016/j.chemgeo.2013.11.006, 2014.

Cumming, G.L., Richards, J.R.: Ore lead isotope ratios in a continuously changing Earth, Earth Planet. Sci. Lett. 150, 277-290, 1975.

Dahl, P.S.: A crystal-chemical basis for Pb retention and fission-track annealing systematics in U-bearing mineral, with implications for geochronology, Earth Planet. Sci. Lett. 150, 277–290, 1997.

Darling, J. R., Storey, C. D. and Engi, M.: Allanite U-Th-Pb geochronology by laser ablation ICPMS, Chem. Geol., 292–293(April 2016), 103–115, doi:10.1016/j.chemgeo.2011.11.012, 2012.

El Korh, A.: Ablation behaviour of allanites during U-Th-Pb dating using a quadrupole ICP-MS coupled to a 193nm excimer laser, Chem. Geol., 371, 46–59, doi:10.1016/j.chemgeo.2014.01.021, 2014.

Elburg, M.A., Bons, P.D., Foden, J., Passchier, C.W.: The origin of fibrous veins: constraints from geochemistry, in: Deformation Mechanisms, Rheology and Tectonics: Current Status and Future Perspectives, Geological Society of London, special publication, Vol. 200, pp. 103-118, 2002.

Enami, M., Liou, J. G. and Mattinson, C. G.: Epidote minerals in high P/T metamorphic terranes: Subduction zone and high- to ultrahigh-pressure metamorphism, Rev. Mineral. Geochemistry, 56, 347–398, doi:10.2138/gsrmg.56.1.347, 2004.

Epin, M. E., Manatschal, G. and Amann, M.: Defining diagnostic criteria to describe the role of rift inheritance in collisional orogens: the case of the Err-Platta nappes (Switzerland), Swiss J. Geosci., 110(2), 419–438, doi:10.1007/s00015-017-0271-6, 2017.

Etheridge, M. A., Wall, V. J. and Vernon, R. H.: The role of the fluid phase during regional metamorphism and deformation, J. Metamorph. Geol., 1(3), 205–226, doi:10.1111/j.1525-1314.1983.tb00272.x, 1983.

Franz, G. and Liebscher, A.: Physical and Chemical Properties of the Epidote Minerals-An Introduction-, Rev. Mineral. Geochemistry, 56(1), 1–81, doi:10.2138/gsrmg.56.1.1, 2004.

Frei, D., Liebscher, A., Franz, G. and Dulski, P.: Trace element geochemistry of epidote minerals, Rev. Mineral. Geochemistry, 56(January), 553–605, doi:10.2138/gsrmg.56.1.553, 2004.

Froitzheim, N. and Eberli, G. P.: Extensional detachment faulting in the evolution of a Tethys passive continental margin, Eastern Alps, Switzerland, Geol. Soc. Am. Bull., 102(9), 1297–1308, doi:10.1130/0016-7606(1990)102<1297:EDFITE>2.3.CO;2, 1990.

Froitzheim, N., Schmid, S.M. and Conti, P.: Repeated change from crustal shortening to orogen-parallel extension in the Austroalpine units of Graubünden, Eclogae Geologicae Helvetiae, 87(2), 559-612, 1994.

Froitzheim, N. and Manatschal, G.: Kinematics of Jurassic rifting, mantle exhumation, and passive-margin formation in the Austroalpine and Penninic nappes (eastern Switzerland), Bull. Geol. Soc. Am., 108(9), 1120–1133, doi:10.1130/0016-7606(1996)108<1120:KOJRME>2.3.CO;2, 1996.

Gieré, R. and Sorensen, S. S.: Allanite and other: REE-rich epidote-group minerals, Rev. Mineral. Geochemistry, 56(January 2004), 431–493, doi:10.2138/gsrmg.56.1.431, 2004.

Goncalves, P., Oliot, E., Marquer, D. and Connolly, J. A. D.: Role of chemical processes on shear zone formation: An example from the Grimsel metagranodiorite (Aar massif, Central Alps), J. Metamorph. Geol., 30(7), 703–722, doi:10.1111/j.1525-1314.2012.00991.x, 2012.

Grapes, R. H. and Hoskin, P. W. O.: Epidote group minerals in low-medium pressure metamorphic terranes, Rev. Mineral.
705   Geochemistry, 56(1993), 301–345, doi:10.2138/gsrmg.56.1.301, 2004.

Gregory, C. J., Rubatto, D., Allen, C. M., Williams, I. S., Hermann, J. and Ireland, T.: Allanite micro-geochronology: A LA-ICP-MS and SHRIMP U-Th-Pb study, Chem. Geol., 245(3–4), 162–182, doi:10.1016/j.chemgeo.2007.07.029, 2007.

Gregory, C. J., Rubatto, D., Hermann, J., Berger, A. and Engi, M.: Allanite behaviour during incipient melting in the southern Central Alps, Geochim. Cosmochim. Acta, 84, 433–458, doi:10.1016/j.gca.2012.01.020, 2012.

710   Guillong, M., Meier, D. L., Allan, M. M., Heinrich, C. A. and Yardley, B. W. D.: SILLS: A Matlab-Based Program for the Reduction of Laser Ablation ICP–MS Data of Homogeneous Materials and Inclusions, Mineral. Assoc. Canada Short Course, 40(June 2015), 328–333, 2008.

Guo, S., Ye, K., Yang, Y., Chen, Y., Zhang, L., Liu, J., Mao, Q. and Ma, Y.: In situ Sr isotopic analyses of epidote: Tracing the sources of multi-stage fluids in ultrahigh-pressure eclogite (Ganghe, Dabie terrane), Contrib. to Mineral. Petrol., 167(2),
715   1–23, doi:10.1007/s00410-014-0975-9, 2014.

Halter, W. E., Pettke, T., Heinrich, C. A. and Rothen-Rutishauser, B.: Major to trace element analysis of melt inclusions by laser-ablation ICP-MS: Methods of quantification, Chem. Geol., 183(1–4), 63–86, doi:10.1016/S0009-2541(01)00372-2, 2002.

Handy, M.R., Herwegh, M., Kamber, B.S., Tietz, R. and Villa, I.M.: Geochronologic, petrologic and kinematic constraints
720   on the evolution of the Err-Platta boundary, part of a fossil continent-ocean suture in the Alps (eastern Switzerland), Schweizerische Mineral. und Petrogr. Mitteilungen, 76, 453-474, 1996.

Herwegh, M., Berger, A., Baumberger, R., Wehrens, P. and Kissling, E.: Large-Scale Crustal-Block-Extrusion During Late Alpine Collision, Sci. Rep., 7(1), 1–10, doi:10.1038/s41598-017-00440-0, 2017.

Herwegh, M., Berger, A., Glotzbach, C., Wangenheim, C., Mock, S., Wehrens, P., Baumberger, R., Egli, D. and Kissling,
725   E.: Late stages of continent-continent collision: Timing, kinematic evolution, and exhumation of the Northern rim (Aar Massif) of the Alps, Earth-Science Rev., 200(November 2019), 102959, doi:10.1016/j.earscirev.2019.102959, 2020.

Hofmann, B. A., Helfer, M., Diamond, L. W., Villa, I. M., Frei, R. and Eikenberg, J.: Topography-driven hydrothermal breccia mineralization of Pliocene age at Grimsel Pass, Aar massif, Central Swiss Alps, Schweizerische Mineral. und Petrogr. Mitteilungen, 84(3), 271–302, 2004.

730   Horn, I., Rudnick, R. L. and McDonough, W. F.: Precise elemental and isotope ratio determination by simultaneous solution nebulization and laser ablation-ICP-MS: Application to U-Pb geochronology, Chem. Geol., 164(3–4), 281–301, doi:10.1016/S0009-2541(99)00168-0, 2000.

Horstwood, M. S. A., Košler, J., Gehrels, G., Jackson, S. E., McLean, N. M., Paton, C., Pearson, N. J., Sircombe, K., Sylvester, P., Vermeesch, P., Bowring, J. F., Condon, D. J. and Schoene, B.: Community-Derived Standards for LA-ICP-MS

735   U-(Th-)Pb Geochronology – Uncertainty Propagation, Age Interpretation and Data Reporting, Geostand. Geoanalytical Res., 40(3), 311–332, doi:10.1111/j.1751-908X.2016.00379.x, 2016.

Horwitz, E. P., Dietz, M. L., & Chiarizia, R.: The application of novel extraction chromatographic materials to the characterization of radioactive waste solutions, Journal of Radioanalytical and Nuclear Chemistry 161, 575–583, 1992.

Incerpi, N., Martire, L., Manatschal, G. and Bernasconi, S. M.: Evidence of hydrothermal fluid flow in a hyperextended
740   rifted margin: the case study of the Err nappe (SE Switzerland), Swiss J. Geosci., 110(2), 439–456, doi:10.1007/s00015-016-0235-2, 2017.

Johannes, W.: Beginning of melting in the granite system Qz-Or-Ab-An-H2O, Contrib. to Mineral. Petrol., 86(3), 264–273, doi:10.1007/BF00373672, 1984.

Košler, J.: Laser ablation ICP-MS - A new dating tool in Earth science, Proc. Geol. Assoc., 118(1), 19–24,
745   doi:10.1016/S0016-7878(07)80043-5, 2007.

Li, X. H., Li, Z. X., Li, W. X., Liu, Y., Yuan, C., Wei, G. and Qi, C.: U-Pb zircon, geochemical and Sr-Nd-Hf isotopic constraints on age and origin of Jurassic I- and A-type granites from central Guangdong, SE China: A major igneous event in response to foundering of a subducted flat-slab?, Lithos, 96(1–2), 186–204, doi:10.1016/j.lithos.2006.09.018, 2007.

Ludwig, K. R.: On the treatment of concordant uranium-lead ages, Geochim. Cosmochim. Acta, 62(4), 665–676,
750   doi:10.1016/S0016-7037(98)00059-3, 1998.

Ludwig, K. R.: User's Manual for A Geochronological Toolkit for Microsoft Excel Berkeley Geochronology Center, Options, (5), 2012.

Malaspina, N., Scambelluri, M., Pennacchioni, G. and Spagnolo, C.: Fluid-induced plastic deformation in the crustal Austroalpine system (Western Italian Alps): A petrologic and fluid inclusion analysis, Ital. J. Geosci., 130(1), 61–74,
755   doi:10.3301/IJG.2010.24, 2011.

Manatschal, G. and Nievergelt, P.: A continent-ocean transition recorded in the Err and Platta nappes (Eastern Switzerland), Eclogae Geol. Helv., 90(1), 3–27, 1997.

Manatschal, G., Marquer, D. and Früh-Green, G. L.: Channelized fluid flow and mass transfer along a rift-related detachment fault (Eastern Alps, Southeast Switzerland), Bull. Geol. Soc. Am., 112(1), 21–33, doi:10.1130/0016-
760   7606(2000)112<21:CFFAMT>2.0.CO;2, 2000.

Mcfarlane, C. R. M.: Allanite U–Pb geochronology by 193 nm LA ICP-MS using NIST610 glass for external calibration, Chem. Geol., 438, 91–102, doi:10.1016/j.chemgeo.2016.05.026, 2016.

Mohn, G., Manatschal, G., Masini, E. and Müntener, O.: Rift-related inheritance in orogens: A case study from the Austroalpine nappes in Central Alps (SE-Switzerland and N-Italy), Int. J. Earth Sci., 100(5), 937–961, doi:10.1007/s00531-
765   010-0630-2, 2011.

Nägler, T. F. and Kamber, B. S.: A new silicate dissolution procedure for isotope studies on garnet and other rock forming minerals, Schweizerische Mineral. und Petrogr. Mitteilungen, 76(1), 75–80, doi:10.5169/seals-57688, 1996.

Oberli, F., Meier, M., Berger, A., Rosenberg, C. L. and Gieré, R.: U-Th-Pb and 230Th/238U disequilibrium isotope systematics: Precise accessory mineral chronology and melt evolution tracing in the Alpine Bergell intrusion, Geochim.
770 Cosmochim. Acta, 68(11), 2543–2560, doi:10.1016/j.gca.2003.10.017, 2004.

Odlum, M. L. and Stockli, D. F.: Thermotectonic Evolution of the North Pyrenean Agly Massif During Early Cretaceous Hyperextension Using Multi-mineral U-Pb Thermochronometry, Tectonics, 38(5), 1509–1531, doi:10.1029/2018TC005298, 2019.

Odlum, M. L. and Stockli, D. F.: Geochronologic constraints on deformation and metasomatism along an exhumed mylonitic
775 shear zone using apatite U-Pb, geochemistry, and microtextural analysis, Earth Planet. Sci. Lett., 538, 116177, doi:10.1016/j.epsl.2020.116177, 2020.

Parrish, R. R., Parrish, C. M. and Lasalle, S.: Vein calcite dating reveals Pyrenean orogen as cause of Paleogene deformation in southern England, J. Geol. Soc. London., 175(3), 425–442, doi:10.1144/jgs2017-107, 2018.

Pennacchioni, G. and Cesare, B.: Ductile-brittle transition in pre-Alpine amphibolite facies mylonites during evolution from
780 water-present to water-deficient conditions (Mont Mary nappe, Italian Western Alps), J. Metamorph. Geol., 15(6), 777–791, doi:10.1111/j.1525-1314.1997.00055.x, 1997.

Pettke, T., Diamond, L. W. and Kramers, J. D.: Mesothermal gold lodes in the north-western Alps: A review of genetic constraints from radiogenic isotopes, Eur. J. Mineral., 12(1), 213–230, doi:10.1127/ejm/12/1/0213, 2000.

Pettke, T., Oberli, F., Audétat, A., Guillong, M., Simon, A. C., Hanley, J. J. and Klemm, L. M.: Recent developments in
785 element concentration and isotope ratio analysis of individual fluid inclusions by laser ablation single and multiple collector ICP-MS, Ore Geol. Rev., 44, 10–38, doi:10.1016/j.oregeorev.2011.11.001, 2012.

Picazo, S. M., Ewing, T. A. and Müntener, O.: Paleocene metamorphism along the Pennine–Austroalpine suture constrained by U–Pb dating of titanite and rutile (Malenco, Alps), Swiss J. Geosci., 112(2–3), 517–542, doi:10.1007/s00015-019-00346-1, 2019.

790 Romer, R. L. and Siegesmund, S.: Why allanite may swindle about its true age, Contrib. to Mineral. Petrol., 146(3), 297–307, doi:10.1007/s00410-003-0494-6, 2003.

Quistini, S., Oddone, M., and Villa. I.M.: Sustainability of aquifers in Mali: Sr and Pb isotopic signatures and tritium ages, Abstract, SGI Congress, Pisa, 22-9, p. 25, 2017.

Rehkämper, M. and Mezger, K.: Investigation of matrix effects for Pb isotope ratio measurements by multiple collector ICP-
795 MS: Verification and application of optimized analytical protocols, J. Anal. At. Spectrom., 15(11), 1451–1460, doi:10.1039/b005262k, 2000.

Ricchi, E., Bergemann, C. A., Gnos, E., Berger, A., Rubatto, D. and Whitehouse, M. J.: Constraining deformation phases in the Aar Massif and the Gotthard Nappe (Switzerland) using Th-Pb crystallization ages of fissure monazite-(Ce), Lithos, 342–343, 223–238, doi:10.1016/j.lithos.2019.04.014, 2019.

800   Ricchi, E., Bergemann, C., Gnos, E., Berger, A., Rubatto, D., Whitehouse, M. and Walter, F.: Cenozoic deformation in the Tauern Window (Eastern Alps, Austria) constrained by in-situ Th-Pb dating of fissure monazite, Solid Earth Discuss., 11, 437–467. https://doi.org/10.5194/se-11-437-2020, 2020.

Rolland, Y., Cox, S. F. and Corsini, M.: Constraining deformation stages in brittle-ductile shear zones from combined field mapping and 40Ar/39Ar dating: The structural evolution of the Grimsel Pass area (Aar Massif, Swiss Alps), J. Struct. Geol.,
805   31(11), 1377–1394, doi:10.1016/j.jsg.2009.08.003, 2009.

Romer, R. L.: Lead incorporation during crystal growth and the misinterpretation of geochronological data from low-238U/204Pb metamorphic minerals, Terra Nov., 13(4), 258–263, doi:10.1046/j.1365-3121.2001.00348.x, 2001.

Romer, R. L. and Xiao, Y.: Initial Pb-Sr(-Nd) isotopic heterogeneity in a single allanite-epidote crystal: Implications of reaction history for the dating of minerals with low parent-to-daughter ratios, Contrib. to Mineral. Petrol., 148(6), 662–674,
810   doi:10.1007/s00410-004-0630-y, 2005.

Savastano, V. L. M., Schmitt, R. da S., Araújo, M. N. C. de and Inocêncio, L. C.: Rift brittle deformation of SE-Brazilian continental margin: Kinematic analysis of onshore structures relative to the transfer and accommodation zones of southern Campos Basin, J. Struct. Geol., 94, 136–153, doi:10.1016/j.jsg.2016.11.012, 2017.

Schaltegger, U. and Corfu, F.: The age and source of late Hercynian magmatism in the central Alps: evidence from precise
815   U-Pb ages and initial Hf isotopes, Contrib. to Mineral. Petrol., 111(3), 329–344, doi:10.1007/BF00311195, 1992.

Schmidt, M. W. and Poli, S.: Magmatic epidote, Rev. Mineral. Geochemistry, 56(January 2004), 399–430, doi:10.2138/gsrmg.56.1.399, 2004.

Schneeberger, R., Kober, F., Lanyon, G. W., Mäder, U. K., Spillmann, T. and Blechschmidt, I.: Grimsel Test Site: Revisiting the site-specific geoscientific knowledge, [online] Available from: www.nagra.ch, 2019.
820   Sláma, J., Košler, J., Condon, D. J., Crowley, J. L., Gerdes, A., Hanchar, J. M., Horstwood, M. S. A., Morris, G. A., Nasdala, L., Norberg, N., Schaltegger, U., Schoene, B., Tubrett, M. N. and Whitehouse, M. J.: Plešovice zircon - A new natural reference material for U-Pb and Hf isotopic microanalysis, Chem. Geol., 249(1–2), 1–35, doi:10.1016/j.chemgeo.2007.11.005, 2008.

Smye, A. J., Roberts, N. M. W., Condon, D. J., Horstwood, M. S. A. and Parrish, R. R.: Characterising the U-Th-Pb
825   systematics of allanite by ID and LA-ICPMS: Implications for geochronology, Geochim. Cosmochim. Acta, 135, 1–28, doi:10.1016/j.gca.2014.03.021, 2014.

Spiegel, C., Siebel, W., Frisch, W. and Berner, Z.: Nd and Sr isotopic ratios and trace element geochemistry of epidote from the Swiss Molasse Basin as provenance indicators: Implications for the reconstruction of the exhumation history of the Central Alps, Chem. Geol., 189(3–4), 231–250, doi:10.1016/S0009-2541(02)00132-8, 2002.
830   Stacey, J. S. and Kramers, J. D.: Approximation of terrestrial lead isotope evolution by a two-stage model, Earth Planet. Sci. Lett., 26(2), 207–221, doi:10.1016/0012-821X(75)90088-6, 1975.

Sylvester, P. J.: Laser Ablation ICP-MS Developments and Trends for 2003, Geostand. Geoanalytical Res., 29(1), 41–52, doi:10.1111/j.1751-908x.2005.tb00654.x, 2005.

Storey, C. D., Jeffries, T. E. and Smith, M.: Common lead-corrected laser ablation ICP – MS U – Pb systematics and geochronology of titanite, , 227, 37–52, 2006.

Sylvester, P.: Matrix effects in laser ablation-ICP-MS, in: Laser ablation ICP-MS in the earth sciences: Current practices and outstanding issues, Mineralogical Association of Canada, Vol. 40, 67-78, 2008.

Tannock, L., Herwegh, M., Berger, A., Liu, J., Lanari, P. and Regenauer-Lieb, K.: Microstructural analyses of a giant quartz reef in south China reveal episodic brittle-ductile fluid transfer, J. Struct. Geol., 130(October 2019), 103911, doi:10.1016/j.jsg.2019.103911, 2020a.

Tannock, L., Herwegh, M., Berger, A., Liu, J. and Regenauer-lieb, K.: The Effects of a Tectonic Stress Regime Change on Crustal-Scale Fluid Flow at the Heyuan Geothermal Fault, South China., Tectonophys., 781(July 2019), 228399, doi:10.1016/j.tecto.2020.228399, 2020b.

Tera, F. and Wasserburg, G. J.: U-Th-Pb systematics in three Apollo 14 basalts and the problem of initial Pb in lunar rocks, Earth Planet. Sci. Lett., 14(3), 281–304, doi:https://doi.org/10.1016/0012-821X(72)90128-8, 1972.

Villa, I. M.: Lead isotopic measurements in archeological objects, Archaeol. Anthropol. Sci., 1(3), 149–153, doi:10.1007/s12520-009-0012-5, 2009.

Wehrens, P., Berger, A., Peters, M., Spillmann, T. and Herwegh, M.: Deformation at the frictional-viscous transition: Evidence for cycles of fluid-assisted embrittlement and ductile deformation in the granitoid crust, Tectonophysics, 693, 66–84, doi:10.1016/j.tecto.2016.10.022, 2016.

Wehrens, P., Baumberger, R., Berger, A. and Herwegh, M.: How is strain localized in a meta-granitoid, mid-crustal basement section? Spatial distribution of deformation in the central Aar massif (Switzerland), J. Struct. Geol., 94, 47–67, doi:10.1016/j.jsg.2016.11.004, 2017.

Weis, D., Kieffer, B., Maerschalk, C., Barling, J., De Jong, J., Williams, G. A., Hanano, D., Pretorius, W., Mattielli, N., Scoates, J. S., Goolaerts, A., Friedman, R. M. and Mahoney, J. B.: High-precision isotopic characterization of USGS reference materials by TIMS and MC-ICP-MS, Geochemistry, Geophys. Geosystems, 7(8), doi:10.1029/2006GC001283, 2006.

Williams, I.S.: U-Th-Pb geochronology by ion microprobe, in: Application of microanalytical techniques to understanding mineralizing processes, edited by: McKibben, M.A., Shanks III, W.C., and Ridley, W.I., Reviews in Economic Geology, 7(1), 1-35, 1998.

Wyllie, P. J.: Crustal anatexis: An experimental review, Tectonophysics, 43(1–2), 41–71, doi:10.1016/0040-1951(77)90005-1, 1977.

Zanoni, D., Rebay, G. and Spalla, M. I.: Ocean floor and subduction record in the Zermatt-Saas rodingites, Valtournanche, Western Alps, J. Metamorph. Geol., 34(9), 941–961, doi:10.1111/jmg.12215, 2016.

Table 1: Measurement conditions on Agilent 7900 for U–Th–Pb isotopic data by LA–ICP–MS.

RF power

14 June 2019	23 July 2019	16 January 2020
1280 W	1320 W	1380 W

Fluence (all sessions)

3 J cm^{-2}

Repetition rate (all sessions)

5 Hz

Cell gas flow

14 June and 23 July 2019	16 January 2020
3.0 ml min^{-1} N$_2$ and 350 ml min^{-1} He	3.0 ml min^{-1} N$_2$ and 400 ml min^{-1} He

Sensitivity on mass 232 measured on NIST SRM612 by dynamic ablation (beam size, fluence, repetition rate, scan rate)

14 June 2019	23 July 2019	16 January 2020
4150 cps/ppm (50 µm, 2.5 J cm^{-2}, 5 Hz, 5 µm sec^{-1})	4410 cps/ppm (50 µm, 2.5 J cm^{-2}, 5 Hz, 5 µm sec^{-1})	3590 cps/ppm (50 µm, 2.5 J cm^{-2}, 5 Hz, 5 µm sec^{-1})

232/238 ratio (all sessions)

> 0.97

248/232 ratio (all sessions)

< 0.002

Background (all sessions)

30 sec

Pre-cleaning (beam size in µm)

14 June and 23 July 2019	16 January 2020
10 pulses (64); followed by wait time of 10 s before ablation	10 pulses (30); followed by wait time of 10 s before ablation

Ablation time (beam size in µm)

14 June and 23 July 2019	16 January 2020
40 sec (50)	30 sec (30)

Measured masses (dwell times in msec)	
14 June and 23 July 2019	**16 January 2020**
204 (40), 206 (40), 207 (40), 208 (40), 232 (40), 238 (40)	206 (40), 207 (40), 208 (40), 232 (40), 238 (40)

Primary reference material (all sessions)

Tara allanite

Secondary reference materials

14 June 2019	**23 July 2019 and 16 January 2020**
CAP[b] allanite	CAP and AVC allanites

Table 2: Reference data of Tara allanite for normalization of U–Th–Pb isotopic data by LA–ICP–MS, and published U–Pb Tera–Wasserburg ages of CAP[b], CAP and AVC allanite secondary reference materials. The ratios for Tara allanite are averages calculated from the measurements by Smye et al. (2014) by ID–TIMS; one measurement was excluded (see text). Uncertainties are given in brackets and are calculated as 2 standard errors. Subscript r = radiogenic ratio; subscript i = initial; superscript a = U–Pb age used as reference in this contribution (see Sect. 5.1 for details). (a) = calculated from five ID–TIMS data of Smye et al. (2014), unanchored regression; (b) = from Burn et al. (2017); (c) = from Gregory et al. (2007).

Isotopic ratio	Tara allanite			
$(^{206}Pb/^{238}U)_r$	0.0678 (0.0008)			
$(^{207}Pb/^{235}U)_r$	0.5020 (0.0173)			
$(^{208}Pb/^{232}Th)_r$	0.0195 (0.0021)			
$(^{207}Pb/^{206}Pb)_r$	0.0537 (0.0016)			
$(^{207}Pb/^{206}Pb)_i$	0.866 (0.079)			
Reference age[a]	**Tara allanite**	**CAP[b] allanite**	**CAP allanite**	**AVC allanite**
U–Pb age	420 ± 16 Ma (a)	284.9 ± 2.8 Ma (b)	275.0 ± 4.7 Ma (c)	289.6 ± 5.6 Ma (c)

Table 3: U–Pb LA–ICP–MS ages of allanite secondary reference materials measured in three analytical sessions in this study. Age uncertainties are 95 % confidence. (a) = regression anchored to a $^{207}Pb/^{206}Pb$ value of 0.854 ± 0.015 (275 Ma; Stacey and Kramers, 1975); (b) = unanchored regression.

Sample	**14 June 2019**		**23 July 2019**		**16 January 2020**	
	Regression U–Pb age [Ma]	Weighted average U–Pb age [Ma]	Regression U–Pb age [Ma]	Weighted average U–Pb age [Ma]	Regression U–Pb age [Ma]	Weighted average U–Pb age [Ma]
CAP[b]	284.2 ± 2.6 (a) MSWD = 0.34 274 ± 29 (b) MSWD = 0.33	284.2 ± 2.0 MSWD = 0.34	-	-	-	-

CAP	-	-	288.5 ± 2.9 (a) MSWD = 1.04 286.9 ± 5.2 (b) MSWD = 1.11	288.6 ± 2.3 MSWD = 1.03	283.0 ± 3.4 (a) MSWD = 1.2 299 ± 20 (b) MSWD = 1.14	282.5 ± 3.2 MSWD = 1.2
AVC	-	-	292.4 ± 3.7 (a) MSWD = 0.49 293.2 ± 7.4 (b) MSWD = 0.53	292.2 ± 2.3 MSWD = 0.48	285.2 ± 4.5 (a) MSWD = 0.70 283 ± 16 (b) MSWD = 0.78	285.1 ± 3.5 MSWD = 0.69

880 **Table 4: Concentrations of Pb, Th and U, Th/U and Pb/U ratios, and μ values measured by laser ablation ICP–MS with the trace element protocol in Appendix A. The symbol < is followed by limits of detection (calculated for each element in each measurement individually following the formulation in Pettke et al., 2012). μ values are calculated from total Pb and total U contents by considering an isotopic abundance of 1.4 % for ^{204}Pb and 93 % for ^{238}U. N/A = non-applicable.**

Sample Albula-1 Vein1					
Pb [μg g^{-1}]	Th [μg g^{-1}]	U [μg g^{-1}]	Th/U [-]	Pb/U [-]	$\mu = {}^{238}U/{}^{204}Pb$ [-]
17	0.02	89	0.0002	0.20	360
19	0.04	22	0.002	0.87	81
6.5	<0.03	11	N/A	0.60	120
7.9	0.05	12	0.004	0.66	110
7.9	0.03	8.9	0.004	0.89	80
3.9	<0.01	28	N/A	0.14	510
9.7	<0.005	28	N/A	0.35	210
18	<0.02	7.1	N/A	2.5	28
21	0.03	11	0.003	1.8	39
11	<0.004	16	N/A	0.70	100
8.2	<0.07	11	N/A	0.74	96
8.5	<0.03	3.7	N/A	2.3	31
7.5	<0.05	4.5	N/A	1.7	43
10	<0.05	5.9	N/A	1.7	42
16	<0.04	5.5	N/A	2.8	25
24	<0.06	8.3	N/A	2.9	25
5.7	<0.03	23	N/A	0.25	290
61	<0.01	6.0	N/A	10	6.9
46	<0.005	7.5	N/A	6.1	12
9.0	<0.02	3.7	N/A	2.4	29
6.4	<0.06	12	N/A	0.51	140
8.3	0.01	26	0.0003	0.32	220
7.6	<0.01	27	N/A	0.28	260

Pb [µg g^{-1}]	Th [µg g^{-1}]	U [µg g^{-1}]	Th/U [-]	Pb/U [-]	µ = ^{238}U/^{204}Pb [-]
6.9	<0.01	9.6	N/A	0.72	99
25	<0.003	4.3	N/A	5.9	12

Vein 2

Pb [µg g^{-1}]	Th [µg g^{-1}]	U [µg g^{-1}]	Th/U [-]	Pb/U [-]	µ = ^{238}U/^{204}Pb [-]
44	0.67	26	0.03	1.7	43
64	14	140	0.10	0.46	160
24	4.0	36	0.11	0.69	100

Sample Grimsel-1

Pb [µg g^{-1}]	Th [µg g^{-1}]	U [µg g^{-1}]	Th/U [-]	Pb/U [-]	µ = ^{238}U/^{204}Pb [-]
130	0.12	190	0.001	0.68	100
150	7.6	180	0.04	0.83	85
170	0.15	270	0.001	0.64	110
150	0.99	230	0.004	0.67	110
130	0.47	79	0.01	1.6	44
130	<0.09	130	N/A	1.0	70
150	0.82	350	0.002	0.44	160
97	0.07	60	0.001	1.6	44
170	0.71	130	0.01	1.3	52
87	0.30	140	0.002	0.64	110
170	0.56	240	0.002	0.72	99
150	2.6	100	0.03	1.4	49
170	0.47	220	0.002	0.78	91
93	4.9	100	0.05	0.90	79
190	0.81	140	0.01	1.4	50
78	1.9	160	0.01	0.49	140
180	0.14	260	0.001	0.68	104
93	0.04	54	0.001	1.7	41
150	0.84	140	0.01	1.1	65

Sample Grimsel-2

Pb [µg g^{-1}]	Th [µg g^{-1}]	U [µg g^{-1}]	Th/U [-]	Pb/U [-]	µ = ^{238}U/^{204}Pb [-]
75	0.07	220	0.0003	0.34	210
68	0.27	160	0.002	0.43	170
75	0.20	150	0.001	0.49	140
51	<0.06	120	N/A	0.42	170
62	<0.05	120	N/A	0.53	130

74	0.07	160	0.0004	0.46	150
97	0.11	270	0.0004	0.35	200
95	0.13	270	0.0005	0.36	200
65	0.21	280	0.001	0.23	310
88	<0.02	180	N/A	0.50	140
93	<0.03	110	N/A	0.86	83
75	0.53	535	0.001	0.14	510
62	0.36	310	0.001	0.20	350

Sample Heyuan-1

Pb [μg g^{-1}]	Th [μg g^{-1}]	U [μg g^{-1}]	Th/U [-]	Pb/U [-]	$\mu = {}^{238}U/{}^{204}Pb$ [-]
19	0.48	8.4	0.06	2.2	32
12	0.30	18	0.02	0.68	100
16	0.38	8.7	0.04	1.8	39
15	0.42	8.4	0.05	1.8	39
27	0.67	7.5	0.09	3.6	20
16	0.05	13	0.004	1.2	57
21	17	24	0.70	0.86	82
20	38	34	1.10	0.58	120
26	0.08	18	0.004	1.4	50
17	0.15	7.0	0.02	2.4	29
16	1.4	9.7	0.14	1.7	42
19	0.13	13	0.01	1.5	49
23	18	30	0.62	0.78	90
17	0.12	9.1	0.01	1.8	39
17	1.3	7.0	0.19	2.4	29
24	0.16	14	0.01	1.6	43
22	2.2	9.9	0.22	2.2	32
8.2	0.04	22	0.002	0.37	190
18	0.88	8.3	0.11	2.2	31
12	0.22	2.6	0.08	4.4	16

Table 5: $^{238}U/^{206}Pb$ and $^{207}Pb/^{206}Pb$ ratios, and their uncertainties as 2 standard errors (2 SE) measured by LA–ICP–MS. f$_{206}$ is
885   calculated using the initial $^{207}Pb/^{206}Pb$ indicated by the Tera–Wasserburg diagrams. (a) = 50 μm spot size; (b) = 30 μm spot size.

Sample Albula-1 (a) Vein1					
Analysis	$^{238}U/^{206}Pb$	2 SE	$^{207}Pb/^{206}Pb$	2 SE	f$_{206}$
1	12.05	0.33	0.734	0.015	0.87
2	8.237	0.258	0.765	0.017	0.91

Analysis	$^{238}U/^{206}Pb$	2 SE	$^{207}Pb/^{206}Pb$	2 SE	f_{206}
3	3.953	0.103	0.815	0.016	0.98
4	0.535	0.013	0.8368	0.0067	1.0
5	0.996	0.028	0.841	0.016	1.0
6	0.952	0.025	0.820	0.013	0.98
7	1.691	0.046	0.8225	0.0079	0.99
8	1.707	0.041	0.8216	0.0098	0.98
9	15.33	0.40	0.712	0.013	0.85
10	4.024	0.097	0.7961	0.0069	0.95
11	6.540	0.188	0.787	0.015	0.94
12	11.53	0.29	0.743	0.015	0.89
13	4.710	0.129	0.807	0.019	0.97
14	2.747	0.128	0.802	0.013	0.96
15	2.076	0.056	0.824	0.014	0.99
16	14.77	0.39	0.718	0.016	0.85
17	2.675	0.068	0.810	0.015	0.97
18	6.053	0.253	0.776	0.014	0.93

Vein2

Analysis	$^{238}U/^{206}Pb$	2 SE	$^{207}Pb/^{206}Pb$	2 SE	f_{206}
19	13.59	0.33	0.7332	0.0096	0.87
20	33.24	0.83	0.5858	0.0088	0.69
21	18.46	0.44	0.689	0.0083	0.82
22	8.576	0.213	0.7578	0.0094	0.90

Sample Albula-1 (b)
Vein1

Analysis	$^{238}U/^{206}Pb$	2 SE	$^{207}Pb/^{206}Pb$	2 SE	f_{206}
1	2.762	0.107	0.839	0.025	1.0
2	13.91	0.58	0.737	0.027	0.89
3	5.035	0.213	0.794	0.028	0.96
4	4.102	0.143	0.788	0.013	0.95
5	4.706	0.168	0.799	0.015	0.96
6	8.569	0.338	0.763	0.028	0.92
7	6.510	0.309	0.782	0.025	0.94
8	3.236	0.157	0.778	0.038	0.94
9	14.08	0.62	0.710	0.030	0.85
10	13.37	0.59	0.735	0.032	0.88

Vein2

Analysis	$^{238}U/^{206}Pb$	2 SE	$^{207}Pb/^{206}Pb$	2 SE	f_{206}
11	17.79	0.70	0.686	0.015	0.83
12	21.90	0.81	0.639	0.017	0.77

13	14.99	0.54	0.703	0.015	0.85
14	10.54	0.77	0.740	0.017	0.89
15	9.940	0.356	0.743	0.016	0.89
16	21.70	0.80	0.658	0.018	0.79
17	26.21	0.96	0.639	0.017	0.77
18	7.107	0.263	0.776	0.013	0.93

Sample Grimsel-1 (a)

Analysis	$^{238}U/^{206}Pb$	2 SE	$^{207}Pb/^{206}Pb$	2 SE	f_{206}
1	3.049	0.121	0.7864	0.0047	0.99
2	2.593	0.059	0.7906	0.005	0.99
3	4.929	0.114	0.7867	0.0062	0.99
4	10.33	0.23	0.7738	0.0042	0.97
5	7.896	0.181	0.7774	0.0058	0.97
6	4.268	0.178	0.7888	0.0053	0.99
7	2.443	0.055	0.7895	0.0061	0.99
8	2.189	0.057	0.7887	0.0049	0.99
9	3.615	0.081	0.7898	0.0054	0.99
10	4.429	0.098	0.7867	0.0058	0.99
11	2.789	0.062	0.7915	0.0056	0.99
12	3.542	0.080	0.7896	0.0054	0.99
13	4.647	0.119	0.785	0.0063	0.98
14	1.098	0.024	0.7937	0.0042	1.0
15	4.137	0.098	0.787	0.0045	0.99
16	6.826	0.158	0.7771	0.0048	0.97
17	2.912	0.067	0.7916	0.0045	0.99
18	5.258	0.127	0.7847	0.0048	0.98
19	4.737	0.112	0.7836	0.0058	0.98
20	6.449	0.145	0.7819	0.004	0.98
21	4.746	0.106	0.7941	0.0066	1.0
22	6.020	0.159	0.7843	0.0053	0.98
23	3.862	0.086	0.7877	0.0053	0.99

Sample Grimsel-1 (b)

Analysis	$^{238}U/^{206}Pb$	2 SE	$^{207}Pb/^{206}Pb$	2 SE	f_{206}
1	5.018	0.166	0.7792	0.0096	0.99
2	2.533	0.090	0.7839	0.0094	1.0
3	6.575	0.220	0.785	0.011	1.0
4	2.674	0.086	0.7852	0.0089	1.0
5	5.266	0.180	0.763	0.012	0.97

6	2.089	0.070	0.7777	0.0074	0.99
7	4.640	0.155	0.783	0.011	1.0
8	1.895	0.065	0.7855	0.0091	1.0
9	5.339	0.177	0.7667	0.0085	0.98
10	4.684	0.158	0.781	0.0086	0.99
11	6.973	0.233	0.780	0.011	0.99
12	2.123	0.077	0.7867	0.0085	1.0
13	1.077	0.036	0.7842	0.007	1.0
14	2.168	0.070	0.783	0.01	1.0
15	2.913	0.093	0.7794	0.0085	0.99
16	2.461	0.079	0.7769	0.009	0.99
17	2.685	0.086	0.7874	0.009	1.0
18	2.357	0.078	0.7771	0.0098	0.99
19	3.840	0.131	0.777	0.010	0.99
20	7.032	0.232	0.7703	0.0095	0.98
21	5.862	0.196	0.7687	0.0099	0.98
22	3.611	0.117	0.7763	0.0065	0.99
23	4.572	0.178	0.7781	0.0099	0.99
24	3.636	0.132	0.7779	0.0090	0.99
25	3.347	0.123	0.7804	0.0080	0.99

Sample Grimsel-2 (a)

Analysis	$^{238}U/^{206}Pb$	2 SE	$^{207}Pb/^{206}Pb$	2 SE	f_{206}
1	13.83	0.31	0.7722	0.0058	0.96
2	19.11	0.44	0.7619	0.0059	0.95
3	13.34	0.30	0.7728	0.0061	0.96
4	8.929	0.215	0.7841	0.0055	0.98
5	12.56	0.284	0.7741	0.0066	0.97
6	11.88	0.27	0.7802	0.0069	0.97
7	8.376	0.189	0.7832	0.0068	0.98
8	8.547	0.248	0.7843	0.0061	0.98
9	13.93	0.43	0.7734	0.0062	0.96
10	10.37	0.29	0.7791	0.0061	0.97
11	8.353	0.188	0.7812	0.0060	0.98
12	9.346	0.262	0.7825	0.0068	0.98
13	20.07	0.48	0.7587	0.0070	0.95
14	9.329	0.218	0.7811	0.0065	0.98
15	8.765	0.200	0.7774	0.0063	0.97
16	10.34	0.23	0.7797	0.0071	0.97

	Sample Heyuan-1 (a)				
Analysis	$^{238}U/^{206}Pb$	2 SE	$^{207}Pb/^{206}Pb$	2 SE	f_{206}
1	5.040	0.155	0.764	0.016	0.93
2	3.565	0.108	0.772	0.012	0.94
3	5.907	0.174	0.734	0.017	0.89
4	4.958	0.160	0.757	0.012	0.92
5	2.655	0.071	0.785	0.013	0.96
6	5.244	0.187	0.742	0.012	0.90
7	3.499	0.098	0.764	0.016	0.93
8	6.676	0.209	0.716	0.019	0.87
9	4.409	0.132	0.757	0.013	0.92
10	2.793	0.117	0.777	0.014	0.95
11	9.578	0.349	0.678	0.016	0.82
12	3.772	0.119	0.775	0.016	0.95
13	4.751	0.165	0.759	0.016	0.93
14	5.525	0.217	0.749	0.019	0.91
15	5.827	0.180	0.739	0.017	0.90
16	1.513	0.050	0.797	0.016	0.98
17	2.252	0.081	0.794	0.015	0.97
18	1.570	0.052	0.801	0.016	0.98
19	18.25	0.57	0.596	0.02	0.71
20	1.595	0.064	0.795	0.019	0.97
21	2.453	0.078	0.775	0.017	0.95
22	0.753	0.021	0.805	0.014	0.99
23	1.435	0.047	0.809	0.016	0.99

Table 6: $^{238}U/^{206}Pb$ and $^{207}Pb/^{206}Pb$ ratios measured by solution ICP–MS. Uncertainties are given as 2 standard errors (2 SE).

Sample	$^{238}U/^{206}Pb$	2 SE	$^{207}Pb/^{206}Pb$	2 SE
Albula-1_A	3.67	0.03	0.81319	0.00004
Albula-1_B	3.61	0.04	0.81337	0.00003
Albula-1_C	3.04	0.04	0.81674	0.00003
Albula-1_D	3.08	0.05	0.81674	0.00003

890 Table C1: U–Pb ages of epidote samples with CAP[b] (14 June 2019) and CAP (23 July 2019) allanites as primary reference materials. Measurements are with a 50 μm spot size. Age uncertainties are 95 % confidence.

Sample	14 June 2019	23 July 2019

	Tera–Wasserburg U–Pb age [Ma]	Tera–Wasserburg U–Pb age [Ma]
Albula-1	61.1 ± 2.8 MSWD = 1.6 n = 22	-
Grimsel-1	18.8 ± 4.3 MSWD = 0.78 n = 22	-
Grimsel-2	16.5 ± 3.5 MSWD = 0.39 n = 16	-
Heyuan-1	-	101.7 ± 8.9 MSWD = 0.87 n = 21
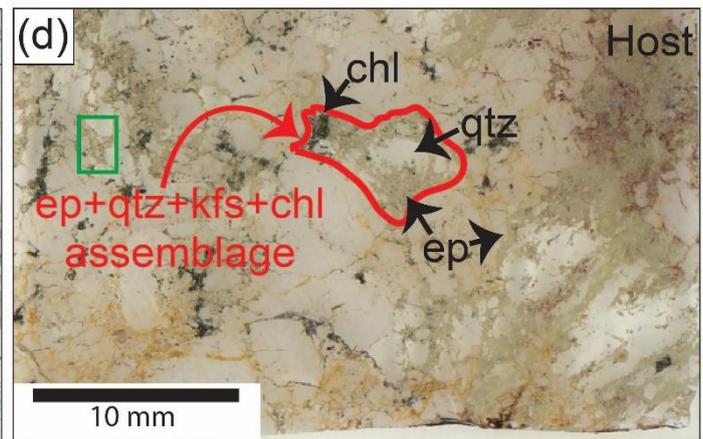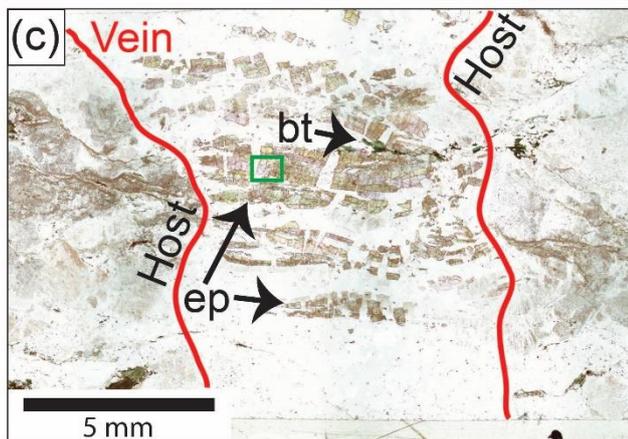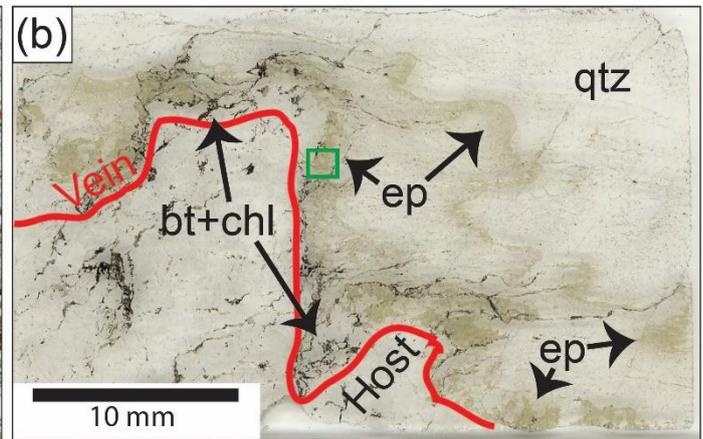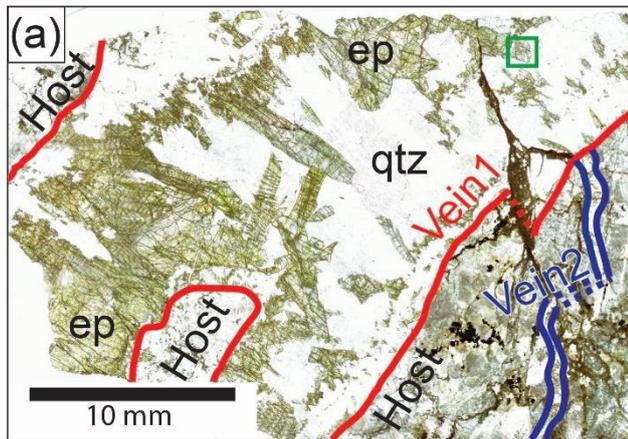
Figure 1: Scans of thin sections of (a) Albula-1, (b) Grimsel-1, (c) Grimsel-2 and (d) Heyuan-1 samples. (a) and (b): plane polarized light on petrographic microscope; (c) and (d): plane light. Green rectangles indicate the location of the BSE images shown in Fig. 2. bt = biotite; chl = chlorite; ep = epidote; kfs = K-feldspar; plg = plagioclase; qtz = quartz.

895
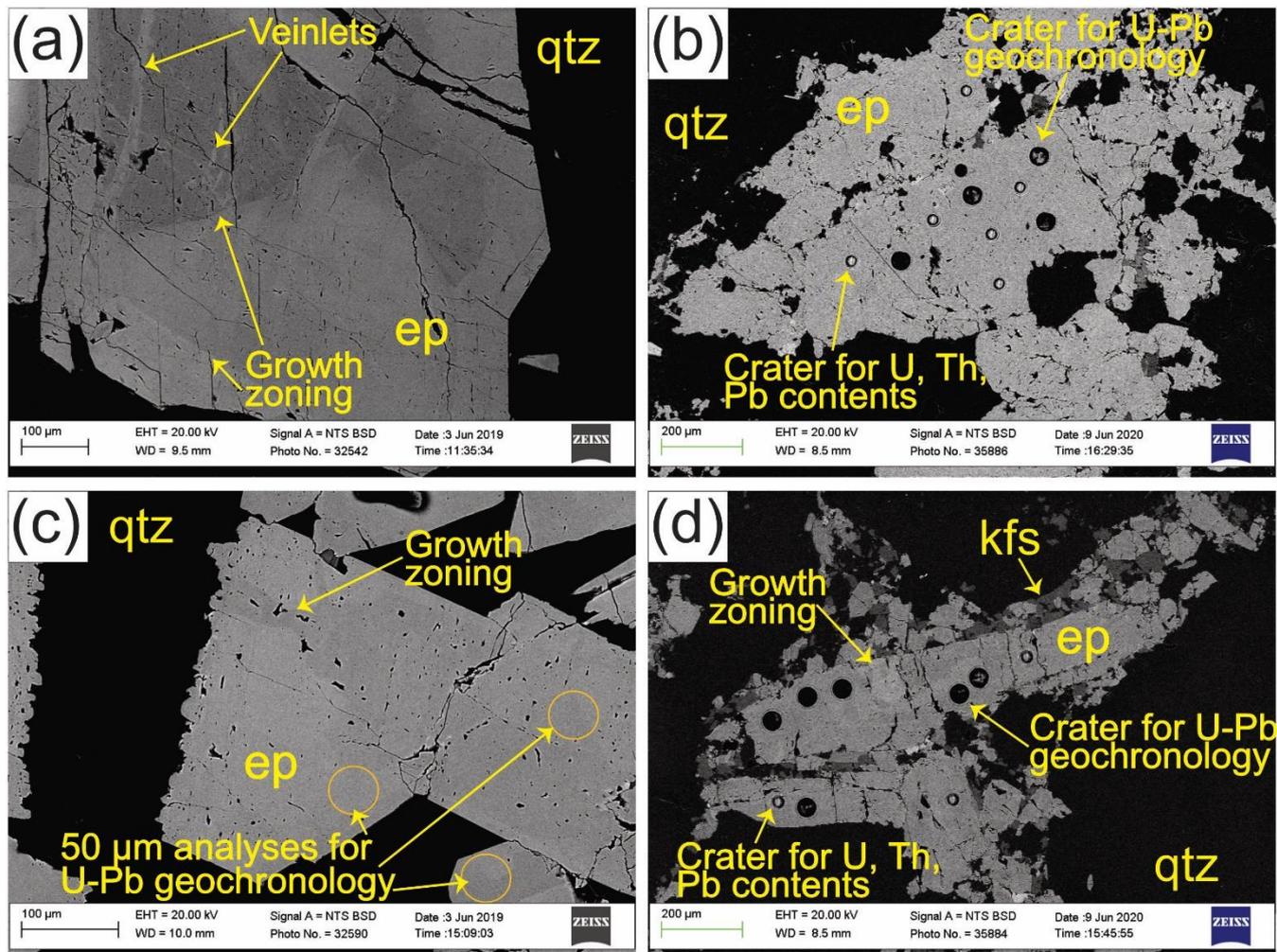
Figure 2: BSE images of (a) Albula-1, (b) Grimsel-1, (c) Grimsel-2 and (d) Heyuan-1 epidote. The specific epidote grain shown in panel (a) was not analyzed. The locations of the BSE images are indicated by the green rectangles in Fig. 1. bt = biotite; chl = chlorite; ep = epidote; kfs = K-feldspar; plg = plagioclase; qtz = quartz.
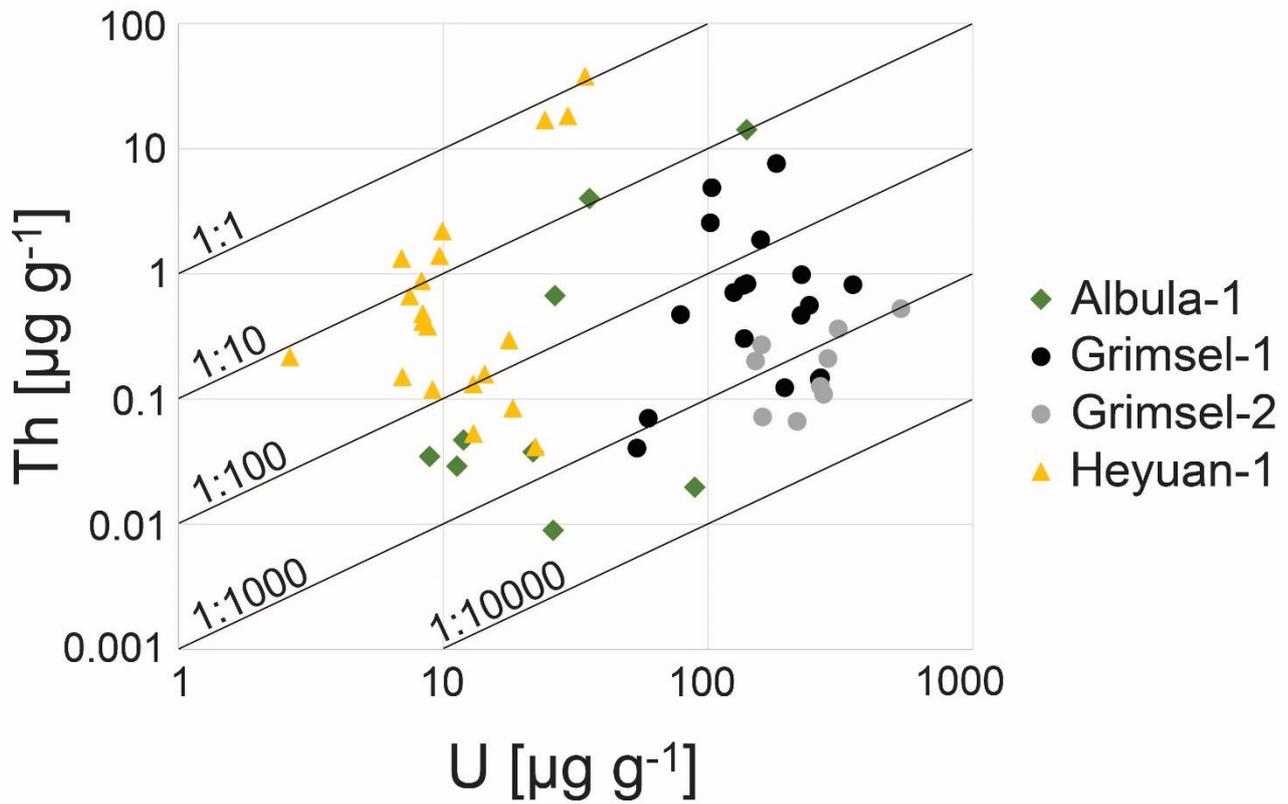
Figure 3: Th and U contents of the analyzed epidote samples.

900
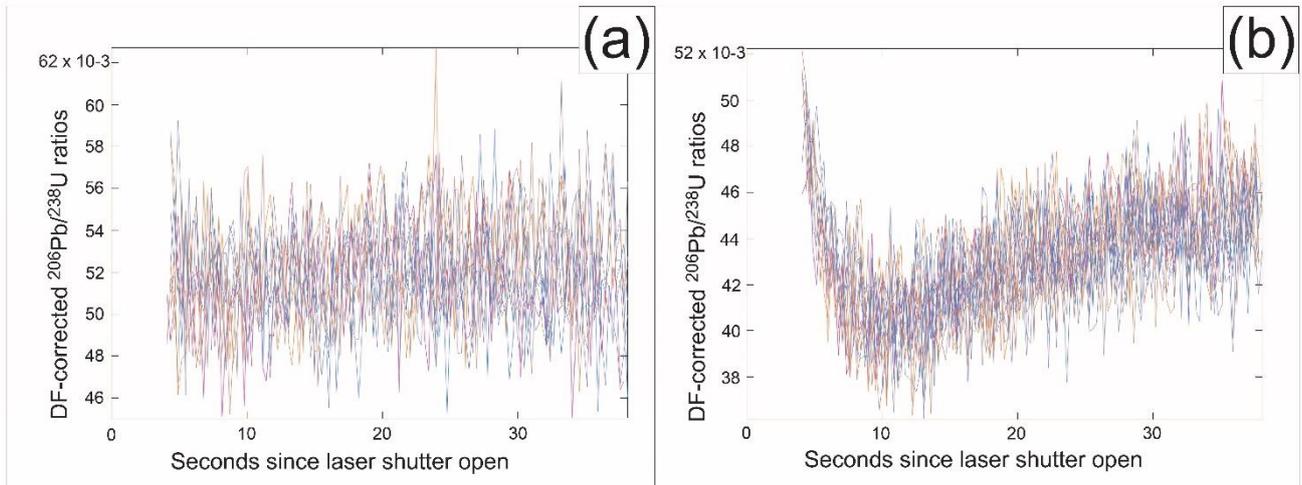
Figure 4: **^{206}Pb/^{238}U ratios measured by LA–ICP–MS corrected for downhole fractionation (DF) of (a) CAP^b allanite and (b) Plesovice zircon with Tara allanite as primary reference material. Each individual line represents one analysis. Measurements are with a 50 μm spot size. The DF-corrected ^{206}Pb/^{238}U ratios include both initial and radiogenic Pb.**
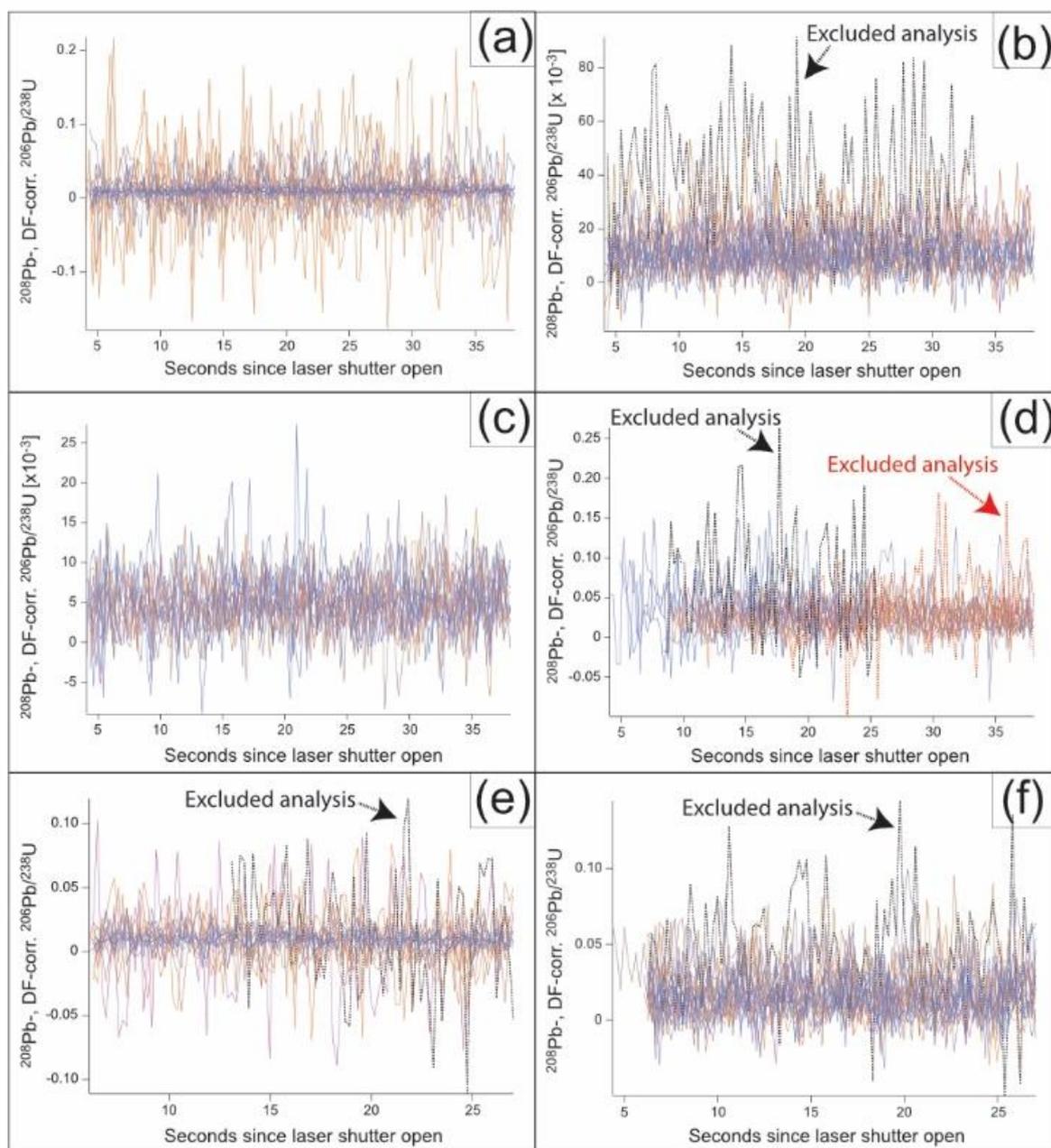
Figure 5: **^{208}Pb-corrected ^{206}Pb/^{238}U ratios measured by LA–ICP–MS corrected for downhole fractionation (DF) of (a) Albula-1, (b) Grimsel-1, (c) Grimsel-2, (d) Heyuan-1, (e) Albula-1 and (f) Grimsel-1 epidote samples with Tara allanite as primary reference material. Each individual line represents one analysis. Measurements are with spot sizes of 50 μm (a-d) and of 30 μm (e-f).**
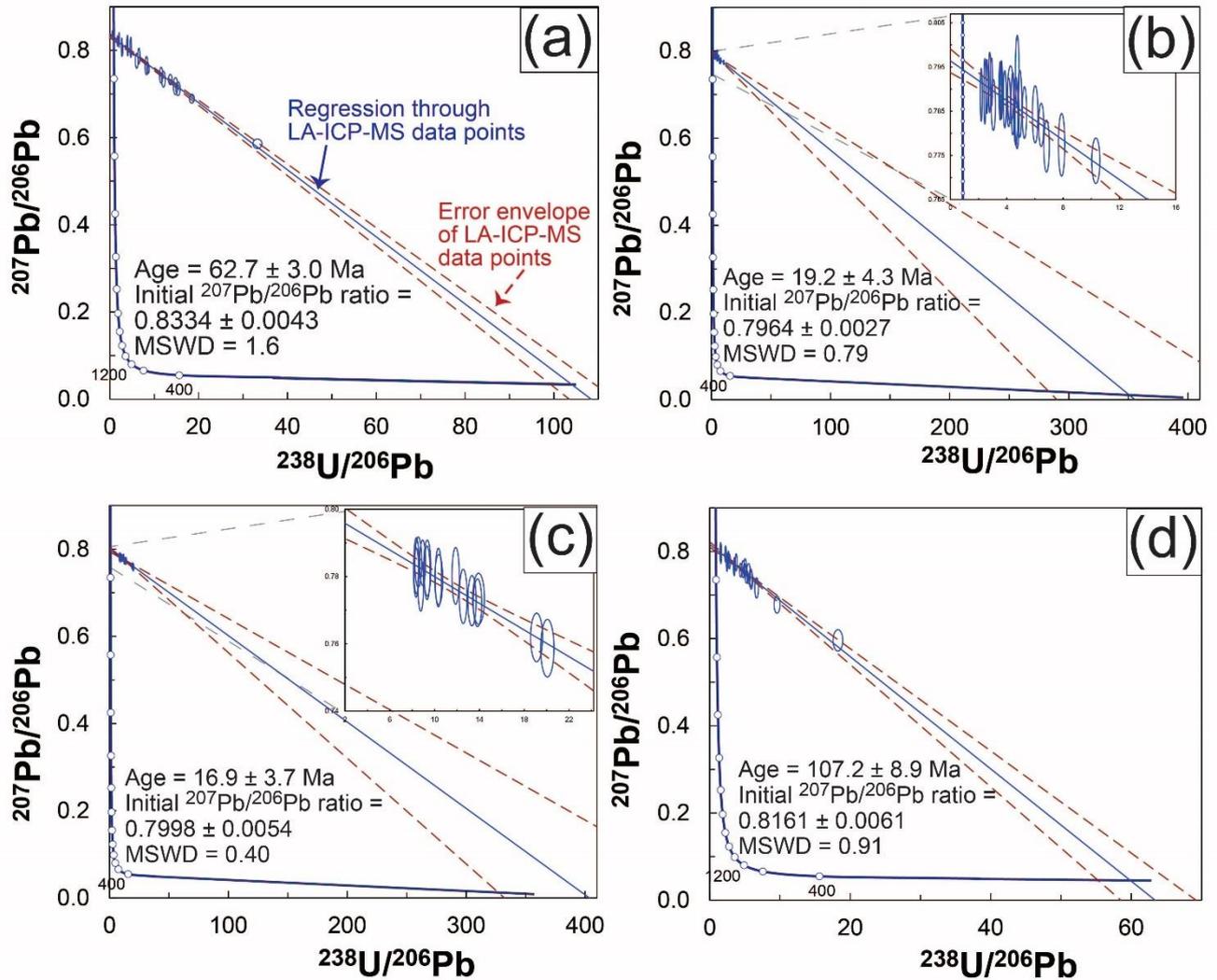
Figure 6: Tera–Wasserburg diagrams of (a) Albula-1, (b) Grimsel-1, (c) Grimsel-2 and (d) Heyuan-1 epidote samples with 50 μm measurements. All ratios are uncorrected for initial Pb. Ages are calculated from the lower intercept of the regressions through the analyses with the concordia, whereas initial $^{207}Pb/^{206}Pb$ ratios are calculated from the upper intercept of the regressions with the y-axis. Data-point error ellipses are 2σ and age uncertainties are 95 % confidence. Error envelopes are plotted with Isoplot 3.7.5 (Ludwig, 2012).
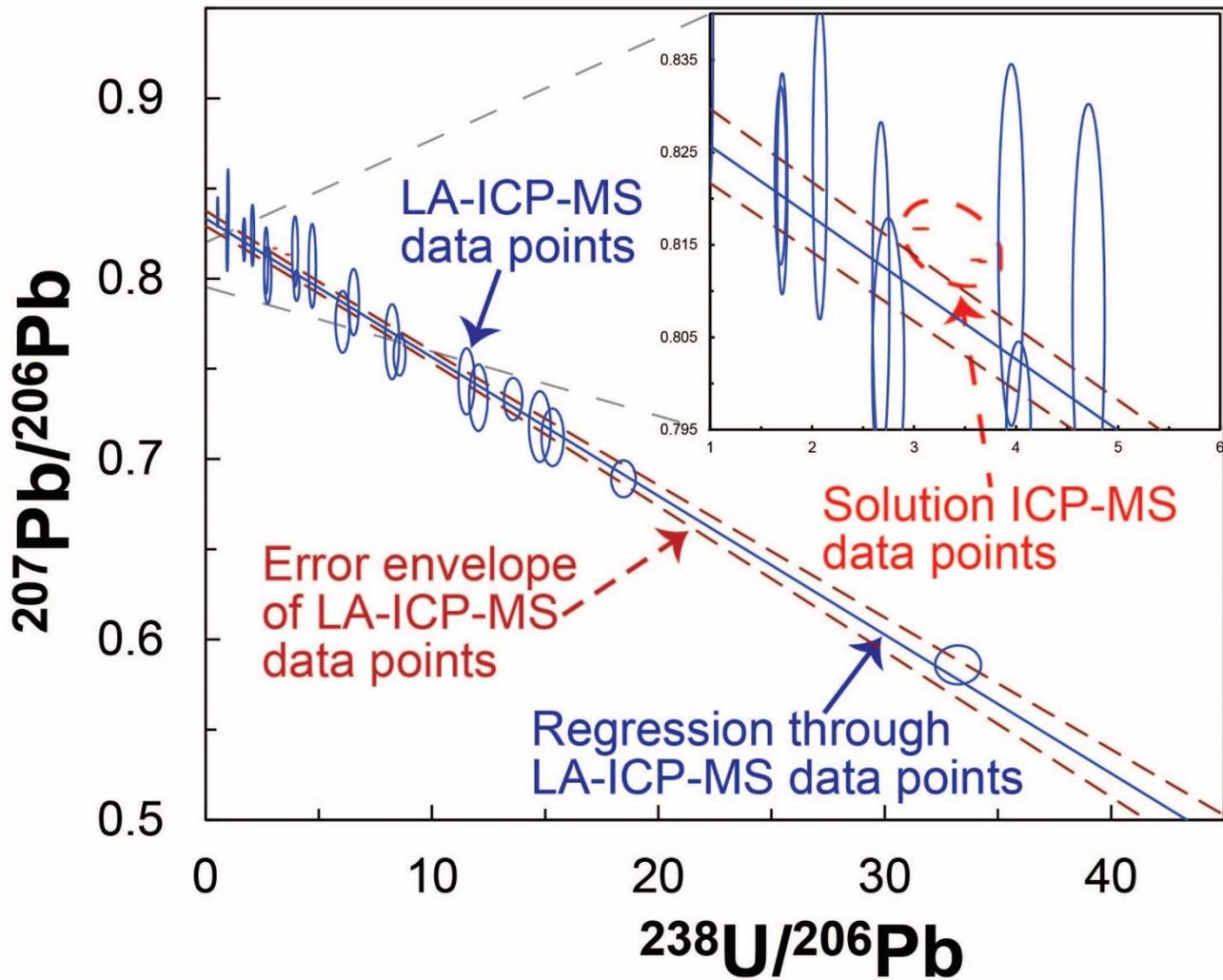
Figure 7: Tera–Wasserburg diagram showing the comparison between laser ablation ICP–MS and solution ICP–MS data points. The error envelope of LA–ICP–MS data points is plotted with Isoplot 3.7.5 (Ludwig, 2012). All ratios are uncorrected for initial Pb. Data-point error ellipses are 2σ.

920
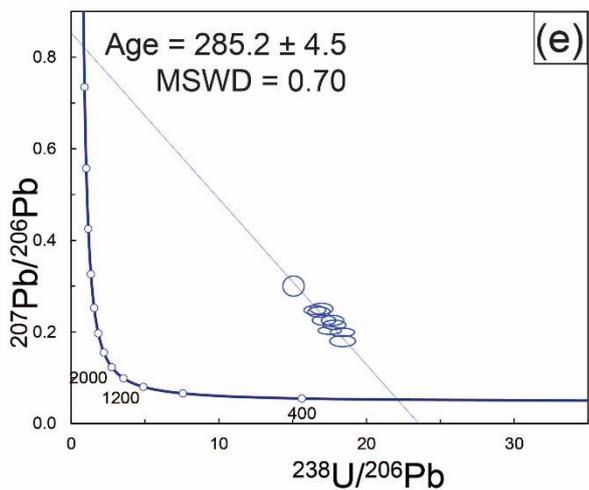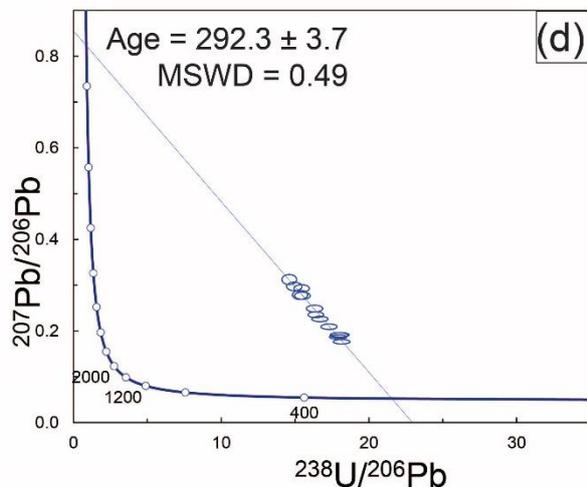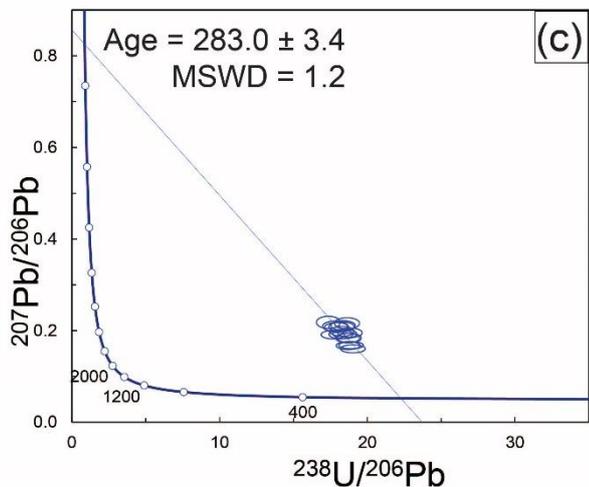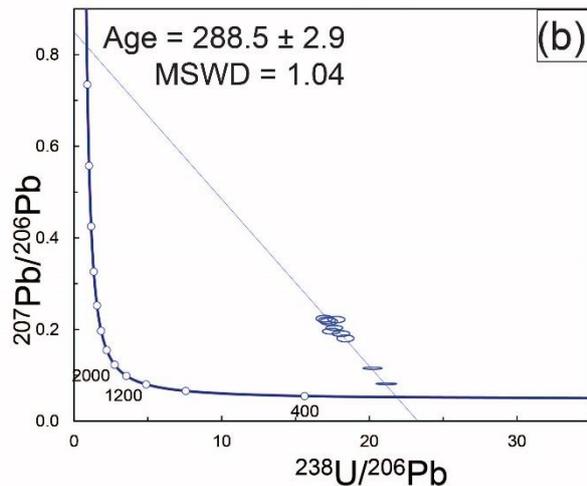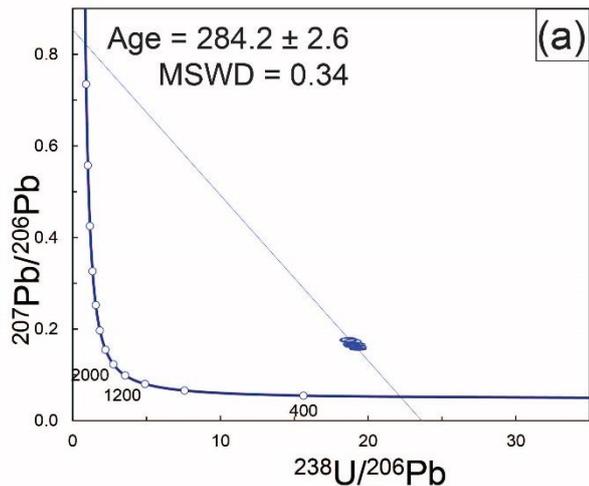
Figure B1: Tera–Wasserburg diagrams of allanite secondary standards. (a) CAP[b] allanite, 14 June 2019 session; (b) CAP allanite, 23 July 2019 session; (c) CAP allanite, 16 January 2020 session. (d) AVC allanite, 23 July 2019 session; (e) AVC allanite, 16 January 2020 session. All ratios are uncorrected for initial Pb. Data-point error ellipses are 2σ and age uncertainties are 95 % confidence.

925